

An observationally based wind model contemporaneous with the radio detections in τ Boötis.

D. Evensberget ¹★, A. A. Vidotto ¹, F. Elekes ^{1,2}, S. Jeffers ³ and R. Luisman¹

¹*Leiden Observatory, Leiden University, PO Box 9513, 2300 RA Leiden, The Netherlands*

²*Institute of Geophysics and Meteorology, University of Cologne, Pohligrstr. 3, 50969 Köln, Germany*

³*Max Planck Institute for Solar System Research, Justus-von-Liebig-Weg 3, 37077, Göttingen, Germany*

Accepted XXX. Received YYY; in original form ZZZ

ABSTRACT

Recent low-frequency array (LOFAR) radio signal detections from the direction of the τ Boötis system have been cautiously attributed to wind-planet interactions between the F6V dwarf τ Boötis A and its hot-Jupiter type exoplanet τ Boötis Ab. We present, for the first time, a stellar surface magnetic map and three-dimensional numerical wind model and planetary magnetosphere model based on spectropolarimetric observations of τ Boötis A made at the same time as the LOFAR observations. The contemporaneous wind models allow us to investigate suggested radio emission mechanisms in the τ Boötis system at the time of the radio signal detections. As exoplanet radio emission mechanisms are sensitive to both the magnetic field geometry of the star-planet system and the he power of the stellar wind in which the exoplanet is embedded, we make full use of our fully three-dimensional magnetohydrodynamical model of the stellar winds in the τ Boötis A system, which extends past the orbit of τ Boötis Ab, and a resolved model of the wind-planet interactions surrounding τ Boötis Ab. Our models indicate that a moderate scaling of the surface magnetic field yield wind energy fluxes of sufficient strength to power the observed radio signals, suggesting that wind variations may explain the intermittent detections.

Key words: stars: planetary systems – stars: low-mass – stars: winds, outflows – planet-star interactions

1 INTRODUCTION

Recently, low-frequency radio signals were detected from the direction the τ Boötis planetary system by Turner et al. (2021). The authors cautiously suggest that the emission originates from the hot Jupiter τ Boötis Ab, which has previously been identified as a favourable candidate for radio emissions (Weber et al. 2018). The signal detections in the 10 MHz to 30 MHz frequency range were conducted with the low-frequency array (LOFAR, van Haarlem et al. 2013).

One of the most likely mechanisms for the radio emission is the interaction between the wind of the host star τ Boötis A and the magnetosphere of the exoplanet τ Boötis Ab. Energetic electrons are thought to emit radio waves via the electron cyclotron-maser instability (ECMI, Siscoe & Chen 1975; Wu & Lee 1979; Hallinan et al. 2015). In the solar system, ECMI emissions have been observed from the auroral regions of the planets (Franklin & Burke 1958; Siscoe & Chen 1975). The ‘radiometric Bode’s law’ (Desch & Kaiser 1984)¹ is a relation between observed radio emissions of the magnetised planets in the solar system and and solar wind dissipated power.

It is natural to ask whether magnetised exoplanets emit at radio frequencies in the same way that solar system planets (e.g., Farrell

et al. 1999; Bastian et al. 2000; Zarka et al. 2001; Lazio et al. 2004). Extrapolations of the radiometric Bode’s law suggest that the emissions of hot Jupiter-type planets can be several orders of magnitude more powerful than those observed in the solar system (Grießmeier et al. 2005, 2007; Vidotto et al. 2010, 2012). If the radiometric Bode’s law and similar scaling relations apply to exoplanetary systems, then the kinetic and magnetic energy fluxes derived from stellar wind modelling can inform the search for exoplanetary radio signals. The wind energy fluxes permit us to estimate the total intensity of the emission. Simple geometrical modelling also permits us to estimate the flux densities that would be observed by radio telescopes.

Radio detection of exoplanets holds great promise as a new method of exoplanet detection (Callingham et al. 2024). Additionally, radio emissions from planetary magnetospheres provide a direct measure of the existence and strength of planetary magnetic fields, which play an important role in planetary energy budgets and habitability (e.g. Lammer et al. 2007; McIntyre et al. 2019). Amplitudes of such interactions also provide information on the energy density of the planet’s space environment, and can thus be used to further constrain stellar winds.

In this work we present a magnetic map of the host star τ Boötis A that is contemporaneous with the radio signal detections reported by Turner et al. (2021). We explore the idea that the emission is being powered by the interaction between the planetary magnetic field and the wind of the host star. By using an Alfvén wave powered, observationally driven three dimensional numerical wind model (Sokolov

★ E-mail: evensberget@strw.leidenuniv.nl

¹ The radiometric Bode’s law should be distinguished from the ‘magnetic Bode’s law’ (Russell 1978), which relates the magnetic field to angular momentum, and the original ‘Bode’s law’ (Bode 1768) which suggested a pattern in the orbital radius of the solar system planets.

et al. 2013; van der Holst et al. 2014), we are able to model the space weather environment of the τ Boötis A system from the stellar chromosphere and past the orbit of τ Boötis Ab.

We use the stellar wind properties at the location of τ Boötis Ab as boundary conditions for a planet-centered magnetohydrodynamical model of the wind-planet interaction.

Our model lets us assess whether the planet is in the sub-Alfvénic or super-Alfvénic regions of the stellar wind, whether the planet's Alfvén wings are connected to the star. With our stellar wind solution we assess the total energy flux of the wind at the position of τ Boötis Ab incident on its magnetosphere and estimate the power of auroral radio emissions powered by the interaction. Lastly we derive associated radio fluxes at the position of the Earth.

This paper is organised as follows: In Section 2 we present the τ Boötis system and the contemporaneous spectropolarimetric observations and radio observations. In Section 3 we present the stellar wind models and the wind-planet interaction model. In Section 4 we present the radio emission mechanisms and the expected radio fluxes. In Section 5 we present the planet-centered magnetohydrodynamical model. In Section 6 we discuss the implications of our results, and in Section 7 we present our conclusions.

2 THE τ BOÖTIS SYSTEM

The τ Boötis system comprises a binary system of an F6V dwarf τ Boötis A and an M2 dwarf τ Boötis B on a wide orbit (Justesen & Albrecht 2019). The system is located at a distance of 15.66(8) pc from the Sun. The primary τ Boötis A has a detected planet, τ Boötis Ab (Butler et al. 1997), which has a semi-major axis of about $7.2R_\star$ (see Table 1). τ Boötis Ab is thought to be tidally locked to τ Boötis A, always presenting the same side towards the star. Furthermore, due to the similarity of the stellar rate of rotation with the orbital period of the planet, the planet is thought to be in synchronous rotation (maintained by tidal interactions) with the star (Shkolnik et al. 2005, 2008) so that the star also always presents the same side towards the planet. Mengel et al. (2016) found, based on spectropolarimetric observations, an equatorial rotation period of 3.20(14) d, and surface differential rotation of up to 20 % was found. The stellar rotation rate at 40° should be equal to the orbital period of the planet (Fares et al. 2009; Mengel et al. 2016). These properties are summarised in the top half of Table 1.

Besides being a hot Jupiter host, the star τ Boötis A is well known for its magnetic polarity reversals (Catala et al. 2007; Donati et al. 2008; Fares et al. 2009) suggesting a rapid magnetic cycle of ~ 240 d (or a multiple thereof such as ~ 720 d) (Fares et al. 2013; Mengel et al. 2016).

The stellar winds of τ Boötis A have been modelled numerically using a polytropic wind with a hot corona (Vidotto et al. 2012; Nicholson et al. 2016) who found wind mass loss rates of $2.3 \times 10^{-12} M_\odot/\text{yr}$ to $2.7 \times 10^{-12} M_\odot/\text{yr}$. Vidotto et al. (2012) also applied a semi-analytical model of planetary auroral radio emissions and showed that τ Boötis Ab could be a strong radio source observable by radio telescopes.

τ Boötis Ab is one of the first discovered exoplanets (Butler et al. 1997), with a radius of $R_p = 1.06^{+0.01}_{-0.02} R_J$ (Wang & Ford 2011), orbiting at a close-in distance of 0.049 au and period 3.3 d (Rosenthal et al. 2021). We adopt the orbital inclination $44.5(15)^\circ$ estimated by Brogi et al. (2012), noting that Rodler et al. (2012) found $47^{+7}_{-6}^\circ$ and that Lockwood et al. (2014) found $45^{+3}_{-4}^\circ$ for this parameter. The dayside surface temperature of τ Boötis Ab is estimated to be 1600 K (Renard et al. 2008), but hydrodynamic escape is not expected

Table 1. Properties of the τ Boötis system. The numbers in the 'ref.' column refer to the following works: 1: Rosenthal et al. (2021), 2: Catala et al. (2007), 3: Mengel et al. (2016), 4: Gaia Collaboration et al. (2023), 5: Wang & Ford (2011), 6: Brogi et al. (2012), 7: Borsa et al. (2015), and 8: Turner et al. (2021).

Star τ Boötis A	Value	Ref.
Radius	R_\star	1.4397(305) R_\odot
Mass	M_\star	1.4032(340) M_\odot
Spin inclination	i_\star	40°
Equatorial rotation period	P_\star	3.20(14) d
Distance from Earth	d_\star	15.66(8) pc
Magnetic field strength	B_\star	1.21 G
		Fig. 2
Planet τ Boötis Ab	Value	Ref.
Orbital period	P_p	3.312 433(19) d
Epoch of periastron	T_p	2 456 400.94(30) d
Semi-major axis	a_p	0.048 69(39) au
Radius	R_p	$1.06^{+0.01}_{-0.02} R_J$
Mass	M_p	4.300(75) M_J
Eccentricity	e_p	$0.007\,40^{+0.005\,90}_{-0.004\,80}$
Inclination	i_p	$44.5(15)^\circ$
Argument of periastron	ω_p	$113.4(322)^\circ$
Time of conjunction	T_{conj}	2 455 652.108(4) d
Magnetic field strength (max)	B_p	8(3) G
		8

due to the planet's high mass and resulting surface gravity (Weber et al. 2018).

Based on the observed frequency ranges, Turner et al. (2021) estimated the polar surface magnetic field strength of τ Boötis Ab to be in the range from 5 G to 11 G. For comparison, Jupiter's polar surface magnetic field strength is ~ 14 G (Acuna & Ness 1976; Connerney 1993). We note that modelling indicates that τ Boötis Ab may have a stronger field than Jupiter, as the planetary magnetic field strength is affected by the stellar energy flux (Christensen et al. 2009; Kilmetis et al. 2024). The planetary parameters adopted in this study are given in the bottom part of Table 1.

2.1 Radio observations of the τ Boötis system

The radio observations we consider in this work comprise seven 2.5 h to 3 h observations of the τ Boötis system made between 18 February 2017 and 25 March 2017 (Appendix A in Turner et al. 2021). Two of these observations, L569131 (2017-02-18) and L570725 (2017-03-06), are tentative detections ascribed to τ Boötis Ab. Of the two observations, L569131 is referred to as a 'bursty' signal reaching an observed flux density of 890^{+690}_{-500} mJy in the 15 MHz to 21 MHz range, while L570725 is a 'slowly varying' emission in the range 21 MHz to 30 MHz range. This signal has an average flux density of 190(30) mJy and a peak flux of 430(30) mJy. The slowly varying signal lasted more than 1 h.

2.2 Contemporaneous spectropolarimetric observations

The contemporaneous magnetic field map of τ Boötis A is constructed based on Zeeman-Doppler imaging (ZDI, Semel 1989), see also Donati & Landstreet (2009). To create the magnetic field map, we conducted spectropolarimetric observations of τ Boötis Ab from 15–22 February 2017, which coincided with the LOFAR observations as indicated in Fig. 1. Our spectropolarimetric observations were obtained with the NARVAL instrument (Aurière 2003) at the Télescope Bernard Lyot. NARVAL is a spectropolarimeter with a resolution $R \sim 65000$ that covers a wavelength range 370 nm to

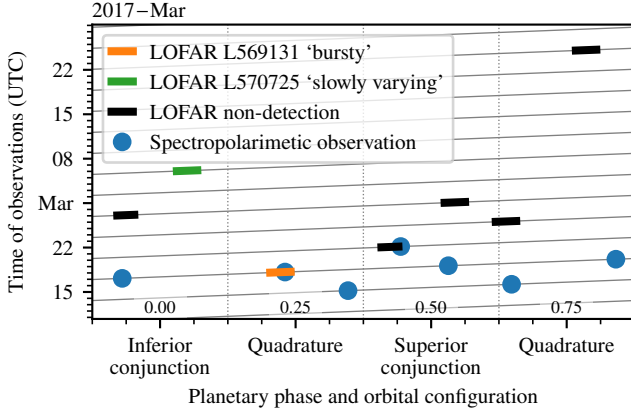


Figure 1. Time and orbital phase of the LOFAR observations of Turner et al. (2021) and the spectropolarimetric observations presented in this work. The orbital configuration is based on the model of Brogi et al. (2012). The planetary configuration is shown as a gray line. The phase is zero at inferior conjunction, which is when τ Boötis Ab is at its closest distance to the observer. The times of spectropolarimetric observations are indicated with blue dots (these times are also given in Table A1). Out of the the LOFAR observations made by Turner et al. (2021), shown as coloured line segments, the ‘bursty’ L569131 signal is contemporaneous with the magnetic observations while the ‘slowly varying’ L570725 signal was observed about two weeks later. The bursty signal was observed near quadrature while the slowly varying signal was observed near the inferior conjunction of τ Boötis Ab.

1050 nm. During the observations, we simultaneously recorded the circularly polarised Stokes V spectrum and the total intensity Stokes I spectrum. We obtain a polarimetric sequence from four consecutive sub-exposures, each of which is taken with a different rotation of the retarder waveplate of the polarimeter relative to the optical axis. The Stokes I spectrum is computed by summing the four sub-exposures, while the Stokes V spectrum from the ratio of sub-exposures with orthogonal polarisation states. A polarimetric sequence lasts 2400 s and comprises 4 sub-exposures of 600 s.

We reduced our data with the LIBRE-ESPRIT pipeline (Donati et al. 1997). At 650 nm, the signal-to-noise ratio per instrument pixel of the circularly polarised spectrum ranges from 1295 to 1559 with an average of 1437. We used a normalising wavelength of 650 nm, and a normalising Landé factor of 1.195.

We applied the least square deconvolution technique (LSD, Donati et al. 1997; Kochukhov et al. 2010) to combine circularly polarised line profiles into a single LSD profile with a high signal-to-noise ratio for each observation. We then combined the set of LSD profiles corresponding to different observations by applying the maximum entropy image reconstruction (Skilling & Bryan 1984) to create the magnetic field map, represented by a set of spherical harmonics coefficients (Jardine et al. 1999; Donati et al. 2006) up to degree $\ell_{\max} = 15$.

As is common in wind modelling, this work only makes use of the radial component of the magnetic field, B_r , which is shown in Fig. 2. The minimum length scale of the magnetic field map is $180^\circ/\ell_{\max} = 12^\circ$ but most of the energy is in lower modes, with 90 % of the energy in modes $\ell \leq 5$ and 99 % of the energy in mode $\ell \leq 8$, giving length scales of 36° and 23° respectively (see Table 3).

The phases and orbital configuration of the τ Boötis system in Fig. 1 is based on the time of conjunction value from Table 1. The studies of Butler et al. (2006); Brogi et al. (2012); Borsa et al. (2015); Rosenthal et al. (2021) suggest that the planetary orbital period (in days) is determined to 5–6 significant digits and it will take decades to

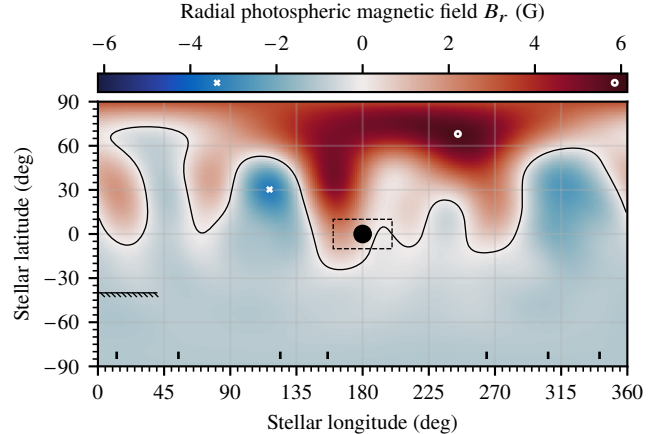


Figure 2. Radial surface magnetic field of τ Boötis A based on spectropolarimetric observations conducted contemporaneously with the detected LOFAR radio signal. The magnetic map shows the radial magnetic field reconstructed with Zeeman-Doppler imaging. The rotation axis of τ Boötis A is inclined by about 40° to the line of sight, hence stellar latitudes below -40° are minimized by the ZDI regularisation. The radial field strength values shown range from -3.38 G to 5.85 G and the mean value of $|B_r|$ is 1.21 G. The location of the minimum and maximum values are indicated by a white cross and a white circle. The location of the planet τ Boötis Ab is indicated by a black dot. The dashed square around the planetary position indicates the longitude and latitude range that will be used for computing quantities at the position of the planet. The phase of the spectropolarimetric observations are indicated by the short tick marks near the longitude axis.

reach an 1 % error in the planetary phase. Thus the error in the planetary phase is insignificant in spite of the large spread in HJD values between the time of conjunction and the times of the observations.

3 STELLAR WIND MODELS

In this section we briefly describe the wind modelling code and the parameter choices we make in this work. We describe the wind models we create and how the parameters vary between the models.

3.1 Wind model software

In this work we obtain steady-state wind solutions by numerically solving the two-temperature MHD equations, extended with heating and cooling terms and two further equations describing the propagation of Alfvén waves energy (AWSOM model, Sokolov et al. 2013; van der Holst et al. 2014). The model is driven by the surface magnetic map shown in Fig. 2. The AWSOM model has been validated for the Sun (Meng et al. 2015; van der Holst et al. 2019; Sachdeva et al. 2019). Many studies have used the model to study the winds of other stars (e.g. Alvarado-Gómez et al. 2016a,b; Cohen 2017; Garraffo et al. 2017; Kavanagh et al. 2021; Evensberget et al. 2021, 2022, 2023; Seach et al. 2022; Marsden et al. 2023; Evensberget & Vidotto 2024; Strickert et al. 2024) The AWSOM model is a component in the block-adaptive tree solarwind Roe upwind scheme (BATS-R-US, Powell et al. 1999; Tóth et al. 2012) code, itself a part of the space weather modelling framework (SWMF, Tóth et al. 2005, 2012; Gombosi et al. 2021). The model equations and parameters used in this work are described in detail in Evensberget et al. (2021, 2022).

Table 2. Model cases considered in this work. Scaling is applied to two parameters; they are the surface magnetic field strength B as shown in Fig. 2 and the Alfvén flux-to-field ratio Π_A/B of Section 3. All other modelling parameters are fixed for the four cases.

Model	ID	B (G)	Π_A/B (W m $^{-2}$ T $^{-1}$)
Unscaled model	B1	1.21	1.1×10^6
10× scaled magnetic field	B10	12.1	1.1×10^6
100× scaled magnetic field	B100	121	1.1×10^6
10× scaled Alfvén wave flux	SA10	1.21	1.1×10^7

The AWSoM module solves numerically for the wind density ρ , wind speed in the stellar frame \mathbf{u} , magnetic field \mathbf{B} , wind thermal pressure p , as well as Alfvén wave energy fluxes propagating along magnetic field lines. The model also includes the effects of electron heat conduction and radiative cooling. The model extends from the stellar chromosphere to planetary distances. The model assumes that the corona is heated by the dissipation of Alfvén wave energy, which is prescribed at the inner boundary of the model, where the Alfvén wave energy input Π_A is proportional to the local value of the magnetic field strength B_r shown in Fig. 2. This is modelled in terms of a proportionality constant Π_A/B . For solar models the value $\Pi_A/B = 1.1 \times 10^6$ W m $^{-2}$ T $^{-1}$ is taken as the default (Gombosi et al. 2018). In this work we consider the solar value and a value ten times larger as can be seen in Table 2 and further expanded below. The wind models presented here were created with the open source version of the SWMF².

3.2 Model parameters

As in Gombosi et al. (2018) and Evensberget et al. (2021, 2022, 2023) we use solar chromospheric temperature $T = 5 \times 10^4$ K and number density values $n = 2 \times 10^{17}$ m $^{-3}$ such that the mass density is $\rho = 3 \times 10^{-10}$ kg m $^{-3}$ at the inner boundary of the model. The radius, mass, and rotation period of τ Boötis A are taken from Table 1 and the references therein. These values are typically applied in the unsaturated regime of stellar X-ray luminosity (see Reiners et al. 2014; Johnstone & Güdel 2015; Alvarado-Gómez et al. 2016a).

To account for uncertainties in the choice of model parameters, we consider four different wind models. As the magnetic field strength found with ZDI may be thought of as a lower bound we create three wind models corresponding to scaling the magnetic field by a factor of 1, 10, and 100. In the following we refer to these models as the B1, B10, and B100 models. We also create a fourth model where the surface Poynting flux is scaled by a factor of 10 (and B is unscaled), which we refer to as the SA10 model. The parameters that we vary between our models are given in Table 2.

3.3 Wind model global results

Fig. 3 shows the coronal magnetic field for the four model cases of Table 2. The field lines and the stellar surface are coloured by the radial field strength. The black circumference indicates the orbital distance of τ Boötis Ab. The system is shown near quadrature, which is the phase of the bursty signal detection (see Fig. 1); the planet is situated in the +x direction, and the observer is situated in the -y direction, looking towards +y (into the paper). The stellar axis of

² The open version of the space weather modelling framework can be found on-line at <https://github.com/MSTEM-QUADA/SWMF.git>.

rotation lies in the x-y plane and is inclined by 40° to the line of sight.

From the indicated field lines, we observe that the region of closed magnetic field lines increases with the magnetic field strength. The orbit of τ Boötis Ab is indicated as a black curve, and the planet is shown (to size) at the position of superior conjunction. The intersection between the Alfvén surface, where the wind speed equals the Alfvén wave speed $u_A = B/\sqrt{\mu_0\rho}$, and the orbital plane of τ Boötis Ab is shown as a green curve. We see that τ Boötis Ab is sub-alfvénic (inside the Alfvén surface) in the B10 and B100 cases, super-alfvénic (outside the Alfvén surface) in the SA10 case, and very close to the Alfvén surface (sometimes called trans-alfvénic) in the B1 case. The ratio between the wind speed and the Alfvén speed has ramifications for the shape of the wind-planet interaction region as discussed in section 3.5.

Table 3 gives aggregate quantities computed from the magnetic map and the resulting wind models. These are provided to enable comparison with other modelling work, in particular Evensberget et al. (2023). In Table 3, the mean and maximum unsigned surface radial field, and the unsigned surface radial flux are computed directly from the magnetic map of Fig. 2. The mean surface field strength, surface field dipole and quadrupole fractions, the poloidal energy quantiles (see Evensberget et al. 2022) are computed at the stellar surface, accounting for the magnetic field in the steady-state wind models (i.e. the radial field is as in Fig. 2 and the perpendicular field values that have settled to their steady state values). The open magnetic flux fraction, open field-line surface fraction, magnetic dipole inclination, average Alfvén radii, and wind mass- and angular momentum-loss rates are computed from the full, steady-state wind model solution as in Evensberget et al. (2021).

The inclination of the magnetic dipole axis with respect to the axis of rotation is between 27° to 30° for the four models. The average Alfvén radius, which we compute in the stellar frame where $u = u_A$, increases with increasing field strength and is the smallest in the SA10 model. We see that the wind mass loss rate is comparable with solar maximum in the B1 model, and appears to scale nearly linearly with both the magnetic field scaling factor and the Poynting flux scaling in the SA10 model. The angular momentum loss rates also increase with increasing B and increasing Poynting flux-to-field ratio Π_A/B as expected.

We note that Poppenhaeger et al. (2010) measured an X-ray flux of 3.21×10^{-12} erg cm $^{-2}$ s $^{-1}$ for τ Boötis. This is equal to a surface X-ray flux of 7.9×10^5 erg cm $^{-2}$ s $^{-1}$. The relation of Wood et al. (2021) suggests that τ Boötis A loses mass via wind at a rate of $\dot{M} \approx 20 M_\odot$. This value is roughly comparable to the B10 case where $\dot{M} = 18.7 M_\odot$ in our models when using the standard solar mass loss rate $\dot{M}_\odot \approx 1 \times 10^9$ kg s $^{-1}$.

3.4 Quantities at the planetary position

To model the radio emission from the planet τ Boötis Ab we need to know the wind parameters at the location of the planet, which requires a model of the planetary orbit. While the planetary orbital phase is known to high accuracy (see Table 1), the rotation period of the star is not as accurately known. Furthermore the differential rotation observed using ZDI (Mengel et al. 2016) introduces some uncertainty about the magnetic field configuration at the sub-planetary point on the star. To account for this we compute planetary quantities in region of azimuthal range ±20 degrees and a polar range ±10 degrees around the expected planetary position. The resulting values and their range are reported in Table 4. This region also indicated by the dashed rectangle in Fig. 2 and Fig. 6.

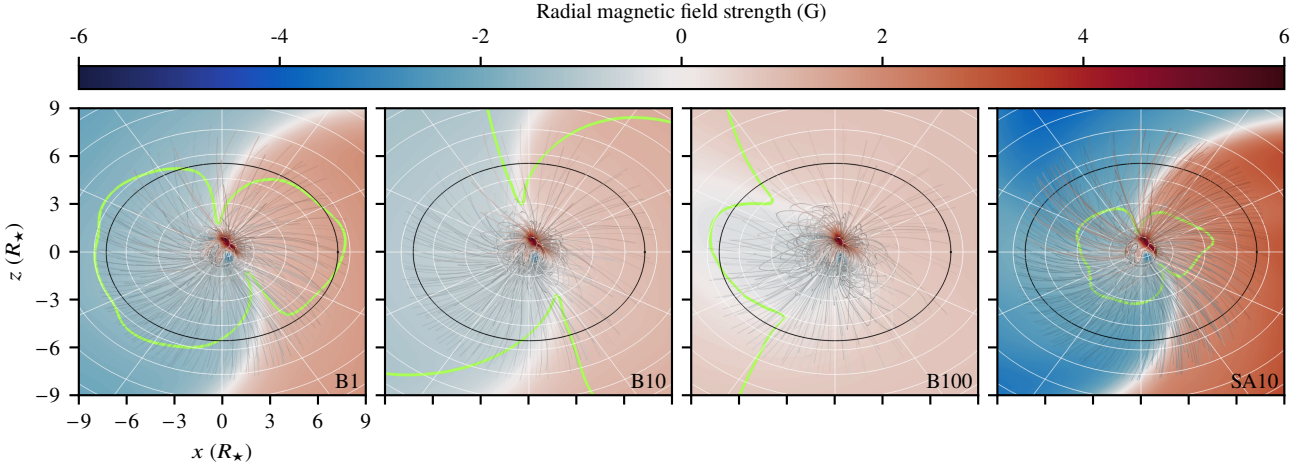


Figure 3. Coronal magnetic field for the four model cases of Table 2. The stellar surface and the orbital plane are coloured by the radial field strength. To enable comparison the magnetic field strength in the B10 and B100 models is scaled with a of 10^{-1} (for the B10 model) and 10^{-2} (for the B100 model). From the indicated field lines we see that the region of closed magnetic field lines increases with the magnetic field strength. The planetary orbital plane and the magnetic field lines are shaded according to a scaled version of the magnetic field strength $B_r (R/R_*)^{2.5}$ to help visualise the field polarity away from the stellar surface. The planetary orbit is indicated as a black circle, and the planet (shown to size at $0.076 R_\star$) may be seen at quadrature along the positive x axis. The intersection of the Alfvén surface and the orbital plane is shown as a green curve. A graticule (white) has been added to help visualise the orbital plane and its inclination to the observer.

Table 3. Aggregate parameters computed from surface magnetic map and the resulting wind models. The ‘Solar’ column refers to the Sun-G2157 solar maximum model of [Evensberget et al. \(2023\)](#) and is included for comparison (note that thermal bremsstrahlung was not computed for the Sun-G2157 model).

Parameter		B1	B10	B100	SA10	Solar
Mean surface radial field strength	(G)	1.19	11.9	119	1.19	5.55
Max surface radial field strength	(G)	5.74	57.4	574	5.74	91.3
Unsigned radial flux at surface	(10^{15} Wb)	1.54	15.4	154	1.54	3.38
Mean surface field strength	(G)	1.69	16.9	170	1.68	9.26
Surface dipole energy fraction	–	0.371	0.374	0.379	0.37	0.006
Surface quadrupole energy fraction	–	0.173	0.173	0.172	0.17	0.0329
Surface energy 90 % length scale	(°)	36	36	36	36	12.9
Surface energy 99 % length scale	(°)	22.5	22.5	22.5	22.5	12
Open magnetic flux fraction	–	0.485	0.326	0.229	0.727	0.468
Open fieldline surface fraction	–	0.336	0.22	0.132	0.411	nan
Magnetic dipole inclination (obliquity)	(deg)	28.5	26.9	27	29.5	66.9
Average Alfvén radius	(R_\star)	6.98	13.1	20	3.73	6.86
Average Alfvén radius in equatorial plane	(R_\star)	5.35	9.88	15.6	2.87	5.36
Wind mass loss rate	(10^9 kg s^{-1})	2.1	18.7	143	28.4	3.84
Wind angular momentum loss rate	(10^{24} N m)	1.28	33.8	480	5.31	2.14
Thermal bremsstrahlung intensity at 10 MHz	(10^{-9} Jy)	0.32	1.83	10.66	0.76	
Thermal bremsstrahlung intensity at 30 MHz	(10^{-9} Jy)	1.25	6.73	52.93	3.32	

Where applicable, the quantities in Table 4 are computed in the planetary frame. For example, the quantity v is the wind speed in the planet’s frame, so that $v = u - u_p$ where u is the wind velocity and u_p is the planet’s orbital velocity in the (non-rotating) stellar frame. This gives a Keplerian velocity $u_p = \sqrt{GM_\star/a_p} = 161 \text{ km s}^{-1}$, where a_p is the semi-major axis of the planet’s orbit (see Table 1). The direction of u_p is such that $\hat{r}_p \times \hat{u}_p = \hat{\Omega}$, where r_p is the vector pointing from the star to the planet. Hence, in every point the planet is assumed to be travelling in the direction of increasing longitude. In our wind model we assume that the orbit of τ Boötis Ab is such that the sub-planet point on the star is stationary.

In the following we discuss the computation of key quantities used to model the radio emission from τ Boötis Ab. These key quantities are also given in Table 4, along with some intermediate values used

in their computation. These intermediate quantities have their usual meaning.

3.5 Size and shape of the planetary magnetosphere

A planetary magnetosphere is the region around a planet which is dominated by the planetary magnetic field ([Chapman & Ferraro 1930](#)). The size of the upstream magnetosphere can be estimated by balancing the total (i.e. thermal, kinetic and magnetic) pressure of the stellar wind p_w with the pressure of the planetary magnetic field p_p ([Chapman & Ferraro 1931](#); [Vidotto et al. 2009](#)). The total wind pressure is calculated at the location of the planet, and in the frame of the planet, from the steady-state numerical wind model (as in e.g. [Vidotto et al. 2011](#))

$$p_w = p + |\mathbf{B}|^2 / (2\mu_0) + \rho_w |v|^2, \quad (1)$$

Table 4. Stellar wind and derived emission-related quantities from the four wind models presented in this work. The listed quantities and their variation were computed in the region indicated by a dashed square in Fig. 6. All quantities are computed in the planetary frame.

Parameter		Unit	B1	B10	B100	SA10
Wind speed	v	(10^6 m s^{-1})	0.453(25)	0.445(11)	0.558(20)	0.440(33)
Density	ρ	($10^{-18} \text{ kg m}^{-3}$)	5.70(79)	53.9(45)	248(37)	77(14)
Magnetic field strength	B	(10^{-6} T)	1.159(41)	7.62(27)	65.4(38)	1.988(61)
Thermal pressure	p	(10^{-6} Pa)	0.0560(13)	0.1386(81)	1.97(41)	0.477(72)
Magnetic pressure	p_B	(10^{-6} Pa)	0.535(37)	23.1(16)	$1.71(20) \times 10^3$	1.574(95)
Ram pressure	p_{ram}	(10^{-6} Pa)	1.157(35)	10.67(64)	77(13)	14.6(10)
Alfvén pressure	p_A	(10^{-6} Pa)	0.2291(91)	0.722(40)	2.87(51)	3.10(14)
Magnetopause radius	R_{mag}	(R_p)	8.355(28)	4.906(41)	2.474(46)	5.910(48)
Obstacle projected area	A_{obs}	(10^{18} m^2)	1.2044(81)	0.4152(70)	0.1056(39)	0.6027(97)
Sound speed	v_s	(10^6 m s^{-1})	0.1288(81)	0.0655(20)	0.1147(34)	0.1021(49)
Alfvén speed	v_A	(10^6 m s^{-1})	0.437(41)	0.928(71)	3.75(49)	0.205(20)
Fast speed	v_{fast}	(10^6 m s^{-1})	0.455(42)	0.931(70)	3.75(49)	0.229(19)
Plasma- β	β	(1)	0.1051(71)	0.00604(72)	0.00120(38)	0.306(63)
Alfvénic Mach number	M_A	(1)	1.043(51)	0.482(29)	0.151(20)	2.16(13)
Fast Mach number	M_{fast}	(1)	0.999(47)	0.480(29)	0.151(20)	1.925(95)
Electron density	n_e	(10^9 m^{-3})	3.41(47)	32.3(27)	148(22)	45.9(84)
Plasma frequency	f_p	(10^6 Hz)	0.0767(52)	0.2363(99)	0.506(38)	0.281(24)
Electron gyrofrequency	f_c	(10^6 Hz)	0.0324(11)	0.2132(76)	1.83(11)	0.0557(17)
Polar cap colatitude		($^\circ$)	6.874(23)	11.76(10)	23.85(47)	9.742(80)
Perpendicular m. field strength	B_{\perp}	(10^{-6} T)	0.798(28)	4.89(12)	28.8(16)	1.441(97)
Wind flow-magnetic field angle	$\angle(\mathbf{v}, \mathbf{B})$	($^\circ$)	43.6(22)	40.0(11)	26.2(21)	46.7(45)
Kinetic radio power	P_k	(10^{15} W)	0.803(63)	10.97(67)	176(14)	1.205(86)
Magnetic radio power	P_{mag}	(10^{15} W)	0.00631(26)	0.0197(13)	0.046(10)	0.0386(37)
Emission cone solid angle	Ω	(sr)	3.69	3.69	3.69	3.69
Radio-magnetic flux	ϕ_k	(mJy)	15.5(12)	212(13)	$3.40(27) \times 10^3$	23.3(17)
Radio-kinetic flux	ϕ_{mag}	(mJy)	0.1219(50)	0.381(25)	0.89(19)	0.747(71)

where the right hand side terms are the thermal pressure p , magnetic pressure p_B , and ram pressure p_{ram} , respectively. It is sometimes assumed that the wind ram pressure dominates the p_w . This holds in the super-alfvénic regime (case B1, SA10) but in the sub-alfvénic regime (case B10, B100) magnetic pressure is the dominant term in the wind pressure (see Table 4).

By assuming that the planet's pressure is magnetically dominated and that its field is dipolar, the planetary pressure acting against the stellar wind is $p_p \simeq (B_p(r/R_p)^{-3})^2/(2\mu_0)$, the distance to the magnetopause³ R_{mag} can be estimated by balancing the wind pressure with the planetary magnetic pressure:

$$R_{\text{mag}}/R_p \simeq (\mu_0)^{-1/6} B_p^{1/3} p_w^{-1/6}, \quad (2)$$

see Appendix D1 for a derivation of this equation. Note that an additional term of order unity is sometimes applied to correct the magnetic field near the magnetopause for the effects of electrical currents in the magnetopause (Cravens 2004).

When a planet is immersed in a supercritical⁴ wind the planet is said to be in the super-alfvénic regime. In this regime the stellar wind is unable to flow around the planetary obstacle in a smooth manner. This causes a bow shock to form on the windwards-facing side of the planetary magnetosphere, where the wind material is rapidly decelerated and deflected. Overall, the planetary magnetosphere takes

³ The magnetopause is the outer edge of the magnetosphere, where the wind pressure is matched by the planetary magnetic pressure.

⁴ In this work we use the term *supercritical* to refer to wind flowing faster than the fastest wave speed in the medium.

on a teardrop shape with a blunt ‘nose’ and a narrow, elongated tail in the supercritical regime (Kivelson & Russell 1995). The orientation of the teardrop shape is determined by the wind velocity in the planetary frame $\mathbf{v} = \mathbf{u} - \mathbf{u}_p$ where \mathbf{u}_p is the planet's orbital velocity in the stellar frame. The size of the magnetosphere as an obstacle to the wind is therefore approximately the area of a circle with radius R_{mag} , where R_{mag} is the distance to the magnetopause.

The fastest magnetohydrodynamical wave is aptly called the ‘fast magnetosonic wave’; it travels at speeds u_{fast} up to $(u_A^2 + c_s^2)^{1/2}$ where $c_s = \sqrt{\gamma p/\rho}$ is the adiabatic sound speed. When the magnetic pressure $p_B \gg p$ dominates the thermal pressure (see eq. 1), $u_A \gg c_s$, and the fast magnetosonic speed $u_{\text{fast}} \approx u_A$. This is known as a low- β plasma, where $\beta = p/p_B$ is the ratio of thermal to magnetic pressure. In low- β plasmas it is common to use the term *super-alfvénic* flow to refer to supercritical flow even though the fast magnetosonic wave speed governs bow shock formation. The values of the parameters discussed here are given in Table 4. We see that plasma- β varies from 0.001 to 0.3 in the four models, with the lowest value in the B100 model and the highest in the SA10 model.

When the speed of the planet through the wind does not exceed u_{fast} and u_A , the planet is said to be in the sub-alfvénic regime. In this scenario MHD waves can propagate upstream and perturb the stellar wind flow, resulting in gradual deceleration of plasma prior to the magnetopause, whereby the magnetopause itself remains the boundary between stellar and planetary magnetic field. In this case Alfvén waves excited by the interaction form, in the planet's frame of reference, standing waves confined to flux tubes originating from the planetary magnetic poles which are referred to as Alfvén

wings (Russell et al. 2016; Saur et al. 2013), which are regions of enhanced magnetic field strength and plasma density (Drell et al. 1965; Neubauer 1998; Saur et al. 2013). The shape of the magnetosphere is determined by the relative orientation of the wind flow, wind magnetic field, and planetary magnetic moment (see e.g. Strugarek et al. 2015; Presa et al. 2024). The topology of the interaction will be investigated further in Section 5.

3.6 Alfvén characteristics

The Alfvén wave energy travels along magnetic field lines with group velocity $\pm \mathbf{u}_A$, where

$$\mathbf{u}_A = \mathbf{B} / \sqrt{\mu_0 \rho}, \quad (3)$$

while the Alfvén waves are simultaneously convected downstream with the wind velocity \mathbf{u} . Consequently, the Alfvén wings are inclined with respect to the background (i.e. stellar) magnetic field. The orientations of the Alfvén wings follow the Alfvén characteristics (e.g. Saur 2018)

$$\mathbf{z}^\pm = \mathbf{u} \pm \mathbf{u}_A. \quad (4)$$

The variables \mathbf{z}^\pm are also known as the Elsasser (1950) variables. Alfvén waves should always be understood as travelling from their origin in both the \mathbf{z}^+ and \mathbf{z}^- directions. We note that for $\mathbf{u} = 0$ the Alfvén characteristics are parallel and antiparallel to \mathbf{B} .

In a compact exoplanetary system such as that of τ Boötis Ab there are two sets of trajectories, analogous to magnetic field lines, that may be traced both forward in time (i.e. in the \mathbf{z}^\pm direction) and backwards in time (in the $-\mathbf{z}^\pm$ direction). Depending on the relative orientation and magnitude of the wind velocity and the Alfvén velocity, several configurations are possible, and the planet may be connected with the star in all four sign combinations if $u < u_A$. On the contrary, when $\mathbf{u} \cdot \mathbf{z}^\pm \geq 0$ and equivalently $u \geq u_A \cos \theta$, Alfvén waves cannot propagate against the wind. Since the wind flow is largely radial, the condition $u \gtrsim u_A \cos \theta$ prevents Alfvén waves from travelling starward.

Alfvén wings are channels of potential star-planet interactions and at the footprints of Alfvén wings, i.e. where the wings intersect the stellar atmosphere, emissions can be excited.

4 RADIO EMISSIONS

To understand the radio emissions from τ Boötis Ab we need to consider the various mechanisms that can produce radio emissions in the system. Exoplanetary radio emissions are categorised into incoherent mechanisms, such as thermal bremsstrahlung and gyroemission, and coherent mechanisms, such as plasmas emissions and electron cyclotron maser emissions, see e.g. Nindos et al. (2008); Callingham et al. (2024). Space weather models permit the modeling of several of the contributing factors of exoplanetary radio emissions, while other factors are determined by microphysical features of the system and modelling that go beyond the magnetohydrodynamical approximation. Nevertheless, the available energy fluxes to power all emissions can be assessed using magnetohydrodynamical models.

Coronal mass ejections, magnetohydrodynamic shocks, and magnetic reconnection can generate plasma emissions, producing type II (minutes-long) and type III (seconds-long) radio bursts and have been modelled by Alvarado-Gómez et al. (2020); Ó Fionnagáin et al. (2022); Strickert et al. (2024), typically to create so-called ‘pseudo-spectra’ that provide emission frequency ranges and time/phase information, but lack quantitative spectral intensity values. Pseudo-spectra

Table 5. Required signal power per steradian for the observed radio signals. The values are computed using eq. 7 and the distance to the τ Boötis system $D = 15.66(8)$ pc from Table 1.

Signal	ϕ (mJy)	Δf (MHz)	$I = P/\Omega$ (W sr $^{-1}$)
L569131	890^{+690}_{-500}	6	$1.25^{+0.96}_{-0.70} \times 10^{16}$
L570725 (peak)	430(30)	9	$9.04(63) \times 10^{15}$
L570725 (mean)	190(30)	9	$3.99(63) \times 10^{15}$

are also often computed for the non-isotropic electron cyclotron instability (ECMI, Twiss 1958; Wu & Lee 1979) emissions, which produce anisotropic radio emissions near the electron cyclotron frequency and its harmonics. The electron cyclotron frequency is given by

$$f_{ce} = \frac{1}{2\pi} \frac{|q_e|B}{m_e} = 2.8 \text{ MHz} \left(\frac{B}{1 \text{ G}} \right) \quad (5)$$

where q_e is the electron charge, B is the local value of the magnetic field strength, and m_e is the electron mass. The direct proportionality between f_{ce} and B means that f_{ce} can be used to probe the magnetic field strength in the emitting region.

Radio signals can only propagate through the wind plasma if the plasma frequency is less than the emission frequency. The plasma frequency is given by

$$f_{pe} = \frac{1}{2\pi} \sqrt{\frac{q_e^2 n_e}{\epsilon_0 m_e}} = 9.0 \text{ Hz} \sqrt{\frac{n_e}{1 \text{ m}^{-3}}} \quad (6)$$

where n_e is the electron number density and ϵ_0 is the electric constant. See Sect. 5 for a discussion on escaping planetary radio emission based on our planetary MHD model. We also note that $f_{pe} \lesssim f_{ce}$ does not hold in at the location of the planet in our B1 model (see Table 4), suggesting that EMCI emissions may not be able to escape from the location of the planet in the B1 case.

4.1 Radio signal strength and energy requirements

The amount of energy flux powering the observed radio signals can be estimated based on the distance to the τ Boötis system and the signal bandwidth. As mentioned in the introduction Turner et al. (2021) observed a bursty signal, L569131, that reached an observed flux of $\phi = 890^{+690}_{-500}$ mJy in the 15 MHz to 21 MHz range, and a slowly varying signal, L570725, with a peak of $\phi = 430(30)$ mJy and average of $\phi = 190(30)$ mJy in the 21 MHz to 30 MHz range.

Following e.g. Farrell et al. (1999), the emitted power P is related to the radio flux by $P = \phi \Delta f D^2 \Omega$ where ϕ is the flux and Δf is the signal frequency range as reported by the radio telescope, D is the distance to the source, and Ω is the solid angle of emission (required since e.g. ECMI is non-isotropic). For the τ Boötis system we have $D = 15.66(8)$ pc from Table 1, which gives

$$I = \frac{P}{\Omega} = \phi \Delta f D^2 \approx \left(\frac{\phi}{10^3 \text{ mJy}} \right) \left(\frac{\Delta f}{1 \text{ MHz}} \right) 2.3 \times 10^{15} \text{ W sr}^{-1} \quad (7)$$

assuming that the signal intensity is constant with respect to frequency. By inspection, equation (7) suggests that the required power per solid angle lies above $\sim 10^{15}$ W sr $^{-1}$; the computed power per solid angle is given in Table 5. In Equation (7) we have applied the definition $1 \text{ Jy} = 10^{-26} \text{ W m}^{-2} \text{ Hz}^{-1}$.

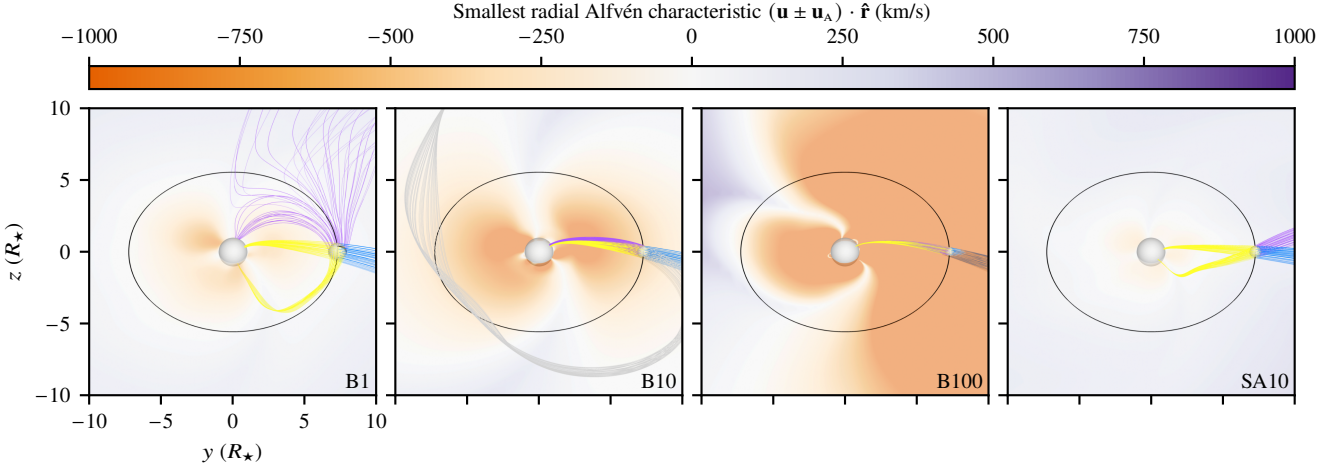


Figure 4. Alfvén characteristic flow lines $\mathbf{u} \pm \mathbf{u}_A$ traced forward in time (blue/purple) and backwards in time (yellow/grey) from their point of intersection with the planetary magnetosphere, represented here as a sphere of radius R_{mag} . The orientation of the system is as in Fig. 3. The equatorial plane is colored by the smallest value of the radial component of $\mathbf{u} \pm \mathbf{u}_A$. The planetary orbit is indicated as a black ellipse. Alfvén wave energy flows towards the planet along the yellow/grey curves, and away from the planet along the (blue/purple) curves.

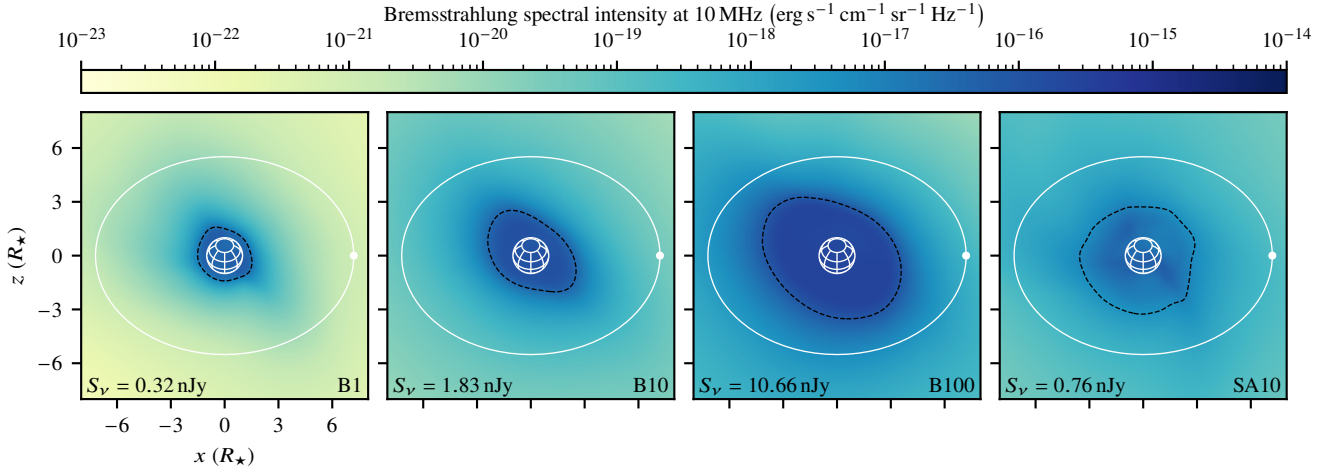


Figure 5. Thermal bremsstrahlung at 10 MHz. The white graticle indicates the star’s position, orientation, and size. The black dashed contour indicates the region for which the wind plasma is optically thick. Notably, the planet is never observed inside or behind the region where the wind plasma is optically thick. A similar figure for thermal bremsstrahlung at 30 MHz is shown in Fig. C1.

4.2 Bremsstrahlung and gyroemission

The stellar wind emits free-free radiation (thermal bremsstrahlung) at radio frequencies. For thermal bremsstrahlung emission the emissivity is often simplified to (e.g. Rybicki & Lightman 1986)

$$\varepsilon_\nu \propto n_e^2 T_e^{-1/2} \exp(h\nu/k_B T_e)$$

where ν is the emission frequency, n_e is the electron density, T_e is the electron temperature. In Fig. 5 we show the thermal bremsstrahlung emission at 10 MHz for the wind models of Table 2, computed using the Radiowinds⁵ code (Ó Fionnagáin et al. 2019; O’Fionnagáin 2021).

In Fig. 5 the black dashed contour indicates the region where the wind plasma is optically thick; we see that τ Boötis Ab never enters

the optically thick region at 10 MHz and thus cannot be said to eclipse the star at 10 MHz. Similarly the planet is not eclipsed by the star due to the system’s rotational inclination (40° , see Table 1). A similar figure for thermal bremsstrahlung at 30 MHz is shown in Fig. C1; here the optically thick region is smaller than at 10 MHz.

Steady-state thermal bremsstrahlung emissions and variations therein induced by transiting planets have been studied by Cohen et al. (2018); Moschou et al. (2018); Ó Fionnagáin et al. (2019). Transiting planets are believed to induce variations in bremsstrahlung radio emissions, which Moschou et al. (2018) found could reach up to unity for certain frequency ranges. The signals strengths of the thermal bremsstrahlung at 10 MHz and 30 MHz are given in Table 3. The values, which are in the nJy range are, however very weak comparison with the observed signals; Pope et al. (2019) suggests that exoplanet radio transits are too weak to be observed even with the next generation of radio telescopes.

Gyroemissions are caused by the gyration of electrons at their

⁵ The Radiowinds code may be found on GitHub at <https://github.com/ofionnad/radiowinds>.

thermal velocities, and is a separate emission mechanism from thermal bremsstrahlung. Gyroemissions in the Sun are primarily associated with active regions and flares, and can be used to gauge their magnetic field strength (White & Kundu 1997; Lee 2007). In the Sun, gyroemissions are generated when hot 10^6 K plasma interacts with strong magnetic fields 100 G or more (Nindos et al. 2019). In the non-flaring Sun, however, the radio emissions come from thermal bremsstrahlung, which tends to dominate over gyroemissions at frequencies up to 3 GHz (White & Kundu 1997). Due to the low frequency ≤ 30 MHz signals considered in this work and dominance of thermal bremsstrahlung below 3 GHz in the Sun, we consider the calculations of gyroemissions to be beyond the scope of this paper and refer the reader to the work of e.g. Fleishman et al. (2021).

4.3 Magnetospheric electron cyclotron maser emissions

The available energy to power magnetospheric emissions is delivered either by the stellar wind or by internal mass transport in rapidly rotating magnetospheres (e.g.; Saur et al. 2021). Close-in exoplanets are, however, expected to rotate slowly due to possible tidal locking with the host star. Therefore we focus on stellar wind-powered, magnetospheric emissions.

Radio observations from Solar system planets suggest that a nearly constant fraction of stellar wind energy incident on the magnetosphere is converted into radio emission generated by the ECMI mechanism (Zarka 2007, 2010; Zarka et al. 2018). The conversion efficiencies from incident kinetic P_k and magnetic power P_B to the power of ECMI-driven radio emission are denoted by η_k and η_B , respectively. It should be noted that these efficiency factors include the efficiencies of energy transfer towards Poynting fluxes in the auroral regions of the planet as well as the efficiency of wave-particle interactions and the ECMI mechanism itself (Elekes & Saur 2023). The difference between the reported η_k and η_B (e.g.; Zarka 2007) comes from the dependence on a generator (i.e. the magnetosphere) to convert mechanical energy to magnetic energy, which strongly depends on the planetary magnetic field strength (Elekes et. al submitted). This additional conversion step causes η_k to be smaller than η_B .

The incident stellar wind energy flux is the sum of thermal, kinetic and magnetic energy flux convected through the effective area of the magnetospheric obstacle, $A_{\text{mag}} = \pi R_{\text{mag}}^2$, where R_{mag} is the radius of the upstream magnetopause. In the following we will neglect the thermal energy flux due to its negligible contribution to the overall incident energy flux. In this work, we adopt two approaches to study planetary radio emission. The first one assesses the radio fluxes generated by stellar wind magnetic and kinetic energy fluxes separately without taking into account the magnetospheric physics. However, in a resolved model, magnetic energy in the planet's auroral regions is generated by the whole stellar wind-planet interaction, incorporating kinetic, magnetic and thermal energy fluxes. We assess this in our second approach, by means of a planetary MHD model in Sect. 5.

4.3.1 Radio power from kinetic interaction

The radio-kinetic emission mechanism is based on assuming the kinetic energy flux across the planetary magnetosphere is the source of power for radio emissions. In a point model this is the flux, with velocity v of wind material with kinetic energy density $e_k = \frac{1}{2}\rho v^2$ over the planetary magnetosphere of cross-sectional area $A_{\text{mag}} = \pi R_{\text{mag}}^2$. This gives an energy flux of $F_k = e_k v$ and power (Vidotto

& Donati 2017).

$$P_k \approx \rho v^3 \pi R_{\text{mag}}^2, \quad (8)$$

where A is the surface of the magnetosphere and \hat{n} is the outward pointing normal vector to the surface. The rightmost expression in eq. (8) is exact when the flux F_k is constant across the magnetosphere and that the the magnetosphere nose is pointed directly windwards.

4.3.2 Radio power from magnetic interaction

In the radio-magnetic emission mechanism the power is assumed to be generated by the interaction between the stellar wind and the planetary magnetic field. By direct analogy with the radio-kinetic mechanism we would consider a magnetic energy density $e_B = B^2/2\mu_0$ being advected at velocity v , resulting in a magnetic energy flux $F_B = e_B v_\perp$,

The available power is, however, computed more accurately based on the Poynting flux of electromagnetic energy, which is given by

$$S = \mu_0^{-1} (\mathbf{E} \times \mathbf{B}).$$

In ideal magnetohydrodynamics we apply Ohm's law $\mathbf{E} = \mathbf{B} \times \mathbf{v}$ to write

$$S = \mu_0^{-1} (\mathbf{B} \times \mathbf{v}) \times \mathbf{B} = \mu_0^{-1} (B^2 v - (\mathbf{B} \cdot \mathbf{v}) \mathbf{B}) = \mu_0^{-1} B^2 v_\perp$$

where v_\perp is the component of the wind velocity perpendicular to the magnetic field. This results in a magnetic power of $P_B \approx \mu_0^{-1} \pi R_{\text{mag}}^2 B^2 v_\perp$.

By integrating S over the projected area of the magnetosphere the Poynting flux is

$$P_B = \int_A S \cdot \hat{n} dA \approx \mu_0^{-1} \pi R_{\text{mag}}^2 B^2 v_\perp. \quad (9)$$

This results differs from the magnetic energy flux by a factor of $2 \sin \theta$, where θ is the angle between the magnetic field and the wind velocity. In our models this difference is between $2 \sin 47^\circ = 1.5$ (for the SA10 model), and $2 \sin 26^\circ = 0.88$ (for the B100 model, see Table 3).

Having estimated the available power P_k and P_B we have to account for the efficiency factors η and solid angle of emission Ω find the intensity values and compare them with the source intensity I values of Table 5, i.e.

$$I_k = \eta_k P_k / \Omega \quad \text{and} \quad I_B = \eta_B P_B / \Omega.$$

when $I \gtrsim I_k$ or $I \gtrsim I_B$ we consider that the radio-kinetic and the radio-magnetic mechanisms are able to power the observed radio emissions.

For the radio-kinetic mechanism, Zarka (2007) estimated that only a fraction $\eta_k = 10^{-5}$ of the kinetic power is converted into radio emissions, and that that fraction $\eta_B = 2 \times 10^{-3}$ of the Poynting flux is converted into radio emissions. In later work Zarka et al. (2018) used $\eta_B = 3 \times 10^{-3}$.

Fig. 6 shows the available power per solid angle I_B (top row) and I_k (bottom row) in a spherical shell at the distance a_p of the planet's orbit for the radio-magnetic interaction model of and the kinetic interaction model. The values are computed from the wind models of Table 2 and the assumptions detailed in the previous sections. All quantities are taken in the planetary frame; in every point the planet is assumed to be travelling in the direction of increasing longitude. The black circle indicates the position of the planet, and the dashed square shape indicates the region where the values of Table 4 are computed.

4.3.3 Solid angle of emission

We account for the anisotropy of ECMI emissions by considering emissions in a double cone pattern (Zarka et al. 2004), and solid angle spanned by the double hollow cone shape is given by (see Appendix E)

$$\Omega = 8\pi \sin \alpha \sin \delta / 2, \quad (10)$$

where α is the cone's half-opening angle and δ is its thickness. Based on solar system considerations, Zarka et al. (2004) used an opening angle α in the range 60° to 90° and the value $\delta = 17.5^\circ$ for the thickness. Applying these values gives Ω ranging from 3.3 sr to 3.8 sr, i.e., the signal is emitted in the direction of 26 % to 30 % of the sky. In the following we will adopt the value $\alpha = 75^\circ$ which gives 29 % sky coverage and $\Omega = 3.7$ sr. We note that a double cone with these parameters is applicable for an unresolved model of ECMI and for broadband signals such as the ones considered in this work (as in e.g. Kavanagh et al. 2019).

A spatially resolved model of the ECMI emission, such as that of Hess et al. (2008, 2010) would use a sum of thinner single cones to model the emission pattern as in the recent work of Zarka et al. (2025). We note that applying the width a thin single cone, e.g. $\delta = 1^\circ$ (Callingham et al. 2024), in an unresolved model would yield $\Omega = 0.21$ sr and a sky coverage of 1.7 %; this amounts to a 17-fold increase in the estimated signal strength.

5 MHD MODEL OF THE PLANETARY MAGNETOSPHERE

In order to study the detailed magnetospheric structure, available energy fluxes converted by the stellar wind-planet interactions and planetary auroral radio emissions, we describe the space environment of τ Boötis Ab and its interaction with the stellar wind by means of a local (e.g. planetary) 3D MHD model. The model presented here is based on the model of Elekes & Saur (2023) and uses the same planetary as well as numerical parameters. The simulations are carried out using the PLUTO (v. 4.4) MHD code. A dipolar planetary magnetic field is assumed with magnetic moment anti-parallel to the stellar rational axis and a polar magnetic field strength of 9 G (Turner et al. 2021). We assume a static, radially symmetric molecular hydrogen atmosphere that acts upon the plasma in terms of sources and sinks of plasma mass, momentum and energy. We consider photo-ionization of neutral particles which is affected by the planetary shadow, charge exchange between ions and neutrals and dissociative recombination. For a detailed description of the planetary MHD model and parametrization of physical processes we refer the reader to Elekes & Saur (2023).

The steady-state stellar wind boundary conditions are obtained from the stellar wind conditions at the orbit of τ Boötis Ab for each stellar wind model separately (see Table 4). We carry out the MHD simulations in spherical coordinates and present the results in a Cartesian system with the x -axis being parallel to the stellar wind velocity in the frame of the planet. The z -axis is perpendicular to the orbital plane and the y -axis completes the left-handed coordinate system.

5.1 Structure of the interaction

In Fig. 8 we show xz -plane cross sections of the simulated planetary magnetosphere. The sub-Alfvénic nature of the stellar wind for models B10 and B100 causes Alfvén wings to develop of which the

northern wing (positive z) connects back to the star while the southern wing is directed away from the star. The super-Alfvénic stellar wind in model SA10 leads to the build-up of a bow shock with a magnetosheath of thickness about $1.5 R_p$. The B1 stellar wind model presents a special case in which the wind is slightly super-Alfvénic ($M_A \approx 1.04$) and slightly sub-fast magnetosonic ($M_{\text{fast}} = 0.99$). The wind in this scenario is thus trans-alfvénic in nature in which degenerate Alfvén wings develop and the upstream stellar wind plasma is perturbed due to fast mode waves. Due to the low stellar wind dynamic pressure the magnetosphere is large, with a stand-off distance of $R_{\text{mag}} \approx 7 R_p$ in the basic B1 and super-Alfvénic model SA10. The enhanced stellar wind magnetic and kinetic pressure in the B10 and B100 model cause the magnetosphere to shrink accordingly to $R_{\text{mag}} < 3 R_p$.

The simulated magnetospheres present a semi-open (i.e. perpendicular) magnetosphere due to the stellar wind magnetic field being nearly perpendicular to the planetary magnetic axis. This geometry results in a weaker magnetic coupling between wind and planetary magnetic field which results in a reduced transfer efficiency from stellar wind energy towards free magnetic energy in the vicinity of the planet. The transfer of energy would be more efficient with a larger stellar wind magnetic field component anti-parallel to the planetary magnetic moment, resulting in an enhanced magnetic reconnection efficiency (Baumjohann & Treumann 2012; Elekes & Saur 2023).

With the northern Alfvén wing being mostly aligned with the stellar wind flow, incident plasma is accumulated within the wing and decelerated by enhanced magnetic pressure and by collisions with neutrals in the ionosphere. The southern wing, on the other hand is not subject to direct plasma injection and thus exhibits a reduced plasma density of about two orders of magnitude lower than the northern wing. This strong asymmetry in plasma density between the southern and northern wing is a consequence of the low inclination between stellar wind flow's velocity and magnetic field so that the wake of the planet lies within the downstream-directed Alfvén wing.

5.2 Auroral radio emissions

For each simulation we compute the total integrated magnetospheric Poynting flux S over a spherical surface with radius $2R_p$ to get a measure of available electromagnetic energy in the auroral regions to power the radio emission. The choice of $2R_p$ is inspired by the electron acceleration regions of Jupiter that typically lie at radii of about $2R_p$ (Zarka 1998). We then calculate the auroral Poynting flux, $S_a = |S \cdot e_{B_0}|$, i.e. the magnetospheric Poynting flux $S = -\mathbf{v} \times \mathbf{B} \times \mathbf{B}$ projected onto the unperturbed dipole field \mathbf{B}_0 (with e_{B_0} being the unit vector along \mathbf{B}_0), and estimate the radio power by multiplication with an auroral radio efficiency factor, ϵ_a . In Elekes & Saur (2023) it is argued that the auroral Poynting flux is an appropriate estimator for electromagnetic energy available to power auroral emissions as it mostly includes Poynting fluxes parallel to auroral magnetic field lines produced by the stellar wind-planet interaction. An important assumption for this calculation is that all Poynting fluxes entering an infinitesimally thin spherical shell with area A are dissipated within the shell to power electron acceleration and the ECMI emission regardless from which direction the Poynting flux is provided. This way we obtain an upper limit auroral Poynting flux. We then obtain the expected radio flux at Earth Φ with

$$\Phi = \frac{\epsilon_a}{\Omega \delta v d^2} \int_A |S \cdot e_{B_0}| dA, \quad (11)$$

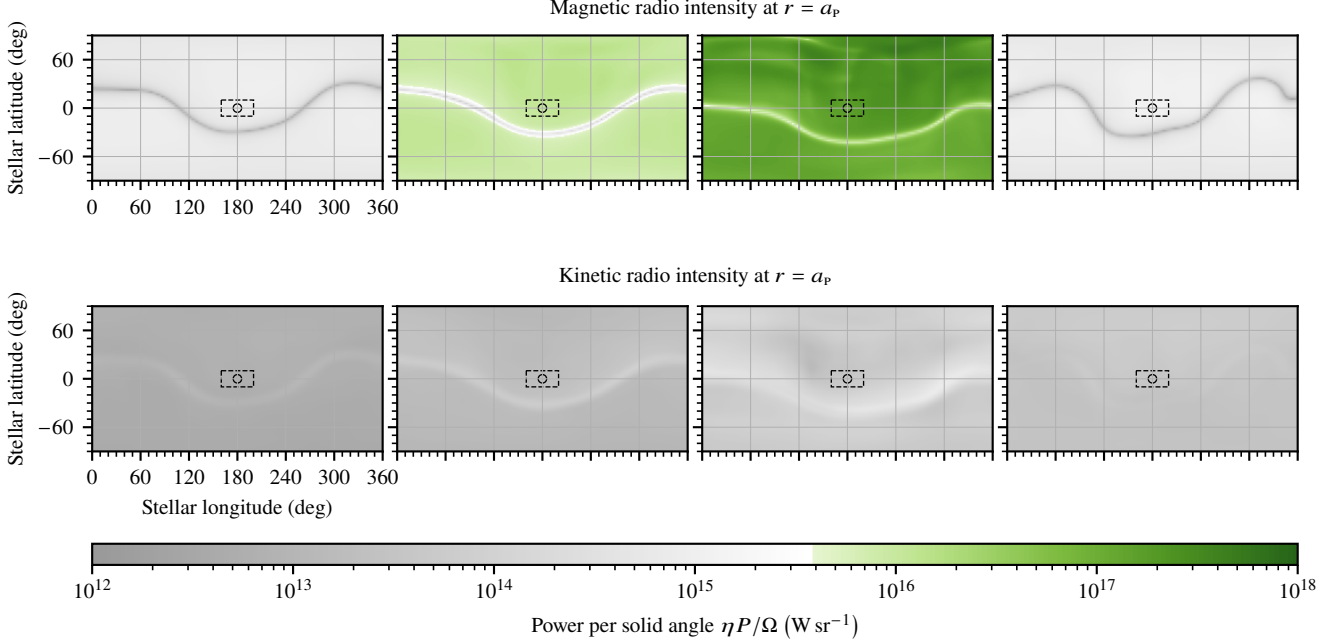


Figure 6. Radio emitted power per steradian $\eta P/\Omega$ for the magnetic and kinetic mechanisms. The values shown are on a spherical shell of radius equal to the orbital distance of τ Boötis Ab. The stellar longitude and latitude values indicate the position of the substellar point. Green values indicate sufficient power available to match the weakest of the radio signals observed by Turner et al. (2021). Wind speeds are calculated in the planetary frame. In every point the planet is assumed to be travelling in the direction of increasing longitude. The black circle indicates the position of the planet, and the black dashed square indicates the area over which the averages in Table 4 are calculated.

Table 6. Magnetospheric Poynting fluxes S , auroral Poynting fluxes S_a and radio fluxes ϕ from the planetary MHD model (Sect. 5). Radio fluxes ϕ are calculated using an auroral Poynting flux-to-radio efficiency of ⁽¹⁾ $\epsilon_a = 3 \times 10^{-3}$ and ⁽²⁾ $\epsilon_a = 10^{-4}$.

Wind model	S (W)	S_a (W)	$\phi^{(1)}$ (mJy)	$\phi^{(2)}$ (mJy)
B1	4.11×10^{19}	1.54×10^{17}	51.9	1.73
B10	3.21×10^{19}	1.97×10^{17}	66.6	2.22
B100	6.11×10^{19}	4.3×10^{17}	145.5	4.85
SA10	1.4×10^{19}	1.38×10^{17}	46.5	1.55

where Ω is the solid angle of the beam, $\delta\nu$ the radio emission bandwidth and $d = 15.6$ pc the distance from the τ Boötis system. We assume the solid angle of the Jovian decametric radio emission, $\Omega = 1.6$ sr (Zarka et al. 2004), and the emission bandwidth to be equal to the maximum gyrofrequency at the poles of τ Boötis b, $\delta\nu \approx 20$ MHz. The radio efficiency factor is poorly constrained but observational evidence exists from Jovian radio emission where ϵ ranges from around 10^{-5} to 10^{-4} (Saur et al. 2021). In this work we consider efficiencies from 10^{-4} to 10^{-3} , which overlaps with the most favorable efficiency range obtained in Elekes & Saur (2023).

Integrated Poynting fluxes and the estimated associated radio fluxes at Earth are summarized in Table 6 and are included in Fig. 7. The radio fluxes presented in Table 6 are calculated with a radio efficiency $\epsilon_a = 10^{-4}$ (similar to Jovian radio emission, e.g.; Saur et al. 2021) and $\epsilon_a = 3 \times 10^{-3}$ (the best case scenario from Elekes & Saur 2023).

For auroral radio emission to escape the source region it is required that the emission frequency (i.e. the local electron gyrofrequency f_c) exceeds the local electron plasma frequency f_p , $f_c > f_p$ (Weber et al.

2017; Treumann 2006) In Fig. 9 we show the ratio f_p/f_c within the planetary magnetosphere in a plane parallel to the planetary magnetic moment. In regions with $f_p/f_c \leq 1$ excited radio emission is likely to escape the planet's vicinity. The sharp contrast of plasma mass density between the northern and southern Alfvén wing consequently leads to an enhanced electron plasma frequency in the northern wing which connects to the star and an extended low frequency region in the southern wing that points away from the star. In the southern wing as well as within the planet's ionosphere the gyro frequency falls mostly below the local plasma frequency and thus we expect most detectable radio emission to originate from the southern polar region of τ Boötis Ab.

6 DISCUSSION

It is intriguing to see the bursty LOFAR signal occurring around quadrature (see Fig. 1), as this configuration has been identified as the most favourable by Kavanagh & Vedantham (2023). To accurately model the effect on system geometry on signal propagation and visibility in ECMI emissions it is required to account for the emission site(s) location, the beaming geometry, and the possibility of occultation by optically thick regions. For a detailed microphysics treatment of EMCI we refer the reader to the work of e.g. Melrose (1989). While detailed modelling of the physics behind these processes is beyond the scope of most wind modelling-based work, the phenomenological modelling of the most relevant physical phenomena involved in EMCI emissions is an area ripe for further exploration.

The efficiency factors η directly affect the radio intensity values shown in Figs. 6–7. In this work we have applied the conservative $\eta_k = 1 \times 10^{-5}$ and $\eta_B = 2 \times 10^{-3}$ values of Zarka (2007) and a more general magnetospheric Poynting flux-to-radio efficiency ϵ_a

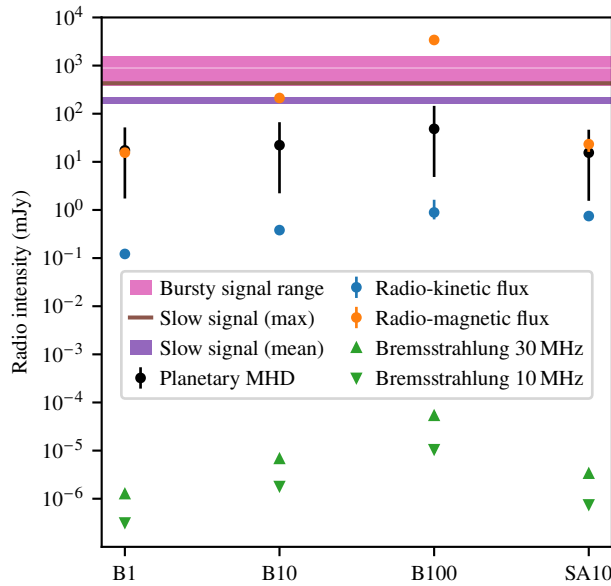


Figure 7. Radio flux densities calculated using the magnetic and kinetic empirical approach (radiometric-Bode's law) and our planetary MHD approach. The coloured bands show the flux intensity ranges reported by LOFAR for the three signals considered in this work. The error bars on the flux values indicate the standard deviation in the computed power in the region indicated by a dashed square in Fig. 6.

(Elekes & Saur 2023) motivated by the Jovian radio aurora (Saur et al. 2021) in the scope of the planetary MHD model (Sect. 5). A larger efficiency factor such as the $\eta = 1 \times 10^{-2}$ used by Turnpenney et al. (2018) would affect the results reported here, increasing the radio intensities by a factor of 5. It should be noted, however, that such high efficiencies are highly unlikely due to the numerous steps involved in converting incident stellar wind energy to auroral radio emission, such as reconnection efficiency, electron acceleration, wave-particle interaction and the ECMI mechanism. A solid angle of emission of $\Omega = 1.6$, see Zarka et al. (2004) would increase radio intensities by a further factor of ~ 2 .

While mathematically distinct, the efficiency factor and beaming factor is not always distinguished in the observational literature. We therefore note that there is significant uncertainty surrounding the appropriate scaling factors to apply for exoplanetary systems.

In the literature estimates have been made for the emissions from τ Boötis Ab. Farrell et al. (1999) suggested that the median flux density should be ~ 2.2 mJy around 28 MHz and pointed to how transient variations in wind strength (speed) and non-isotropic emissions could increase the flux by a factor of 100–1000. Similarly, Grießmeier et al. (2005) suggested that the system should emit with a flux density of 4 mJy to 9 mJy and a frequency 7 MHz to 19 MHz.

A multi-epoch search was conducted by Lazio & Farrell (2007) who did not detect the planet at 74 MHz. This suggests an upper limit on the emitted flux from 135 mJy to 300 mJy. The authors noted that the typical luminosity of the planet should be less than 10^{16} W, unless the solid angle of emission $\Omega \ll 4\pi$.

The recent study by Elekes & Saur (2023) applied a polytropic wind model (Nicholson et al. 2016) to obtain a radio flux $\phi = 300$ mJy only compatible with the observations of Turner et al. (2021) with a magnetospheric Poynting flux-to-radio efficiency $\epsilon_a \geq 10^{-3}$ or a stellar wind density orders of magnitude larger than the density of

the predicted wind (Nicholson et al. 2016). Their result indicates, despite the star-planet interaction being extremely energetic with powers around 10^{18} W to 10^{20} W, that magnetospheric emissions from such close-in exoplanets are barely detectable.

They found the magnetic topology to be the dominant influence on the emission amplitude, followed by the mechanical energy of the stellar wind. In their study Elekes & Saur (2023) simulated an open, semi-open and closed magnetosphere whereby the stellar wind and planetary magnetic field are perfectly anti-parallel in the open magnetosphere scenario. This ideal scenario (based on the modelling choices of Elekes & Saur (2023)) resulted in upper limit radio fluxes due to the geometry being most favourable for magnetic reconnection between stellar wind and planetary magnetic fields.

However, typically stellar wind magnetic field lines have strong radial components and are inclined at angles below 90° with respect to the stellar wind velocity, resulting in a significantly reduced energy transfer efficiency. In this work we used the nearly radial stellar wind magnetic field obtained from the ZDI map and respective stellar wind simulations.

After the radio detections of Turner et al. (2021), which are analysed in this work, there has been multiple non-detections reported (Turner et al. 2023, 2024; Cordin et al. 2025). Several reasons for the non-detections have been proposed, including magnetic cycles in τ Boötis A, unfavourable viewing geometry and beaming conditions, and variations in the magnetosphere of τ Boötis Ab.

In our resolved planetary MHD model (see Section 5) we find the expected radio fluxes to be even further reduced to 1–10 mJy. These radio fluxes lie two orders of magnitude below those derived from a recent planetary MHD model that was based on a super-Alfvenic stellar wind model and in which the same emission characteristics as well as planetary parameters were used (Elekes & Saur 2023; Nicholson et al. 2016). Additionally, the radio fluxes follow more closely the radio-kinetic fluxes obtained using the radiometric Bode law. Increasing the magnetic energy of the stellar wind thus plays a comparably insignificant role in enhancing magnetospheric Poynting fluxes and consequently has a weak effect on auroral radio emissions. This is due to the relatively low efficiency of magnetic reconnection because of the weak stellar wind magnetic field component anti-parallel to the planetary magnetic moment (Baumjohann & Treumann 2012). Magnetospheric Poynting fluxes are additionally generated by mechanical perturbation of the magnetosphere. The inductive response of the magnetospheric plasma then generates free magnetic energy that is transported towards the auroral regions via Poynting fluxes. The mechanical energy of the present stellar wind model, however, is orders of magnitude lower compared, for example, to the previous wind model of τ Boötis Ab (Nicholson et al. 2016; Elekes & Saur 2023). We thus conclude that the steady-state stellar wind presented here does not carry enough energy to power observable radio emission in the range reported by Turner et al. (2021). Although the radio emission in the model presented here is able to escape the magnetosphere, an enhanced stellar wind density might translate to enhanced magnetospheric plasma density which in turn may prohibit the escape of radio emission.

The geometry of the interaction is poorly constrained and, depending on the orientation of the planetary magnetic field with respect to the stellar magnetic field, the resulting radio fluxes might be enhanced considerably. It was previously shown that the radio fluxes increase by slightly from a semi-open towards an open magnetosphere scenario (Elekes & Saur 2023). According to their result the radio fluxes presented here could be enhanced by approximately a factor of 2 in an open-magnetosphere (i.e. best case) scenario, in which planetary and stellar magnetic field are perfectly anti-parallel. This,

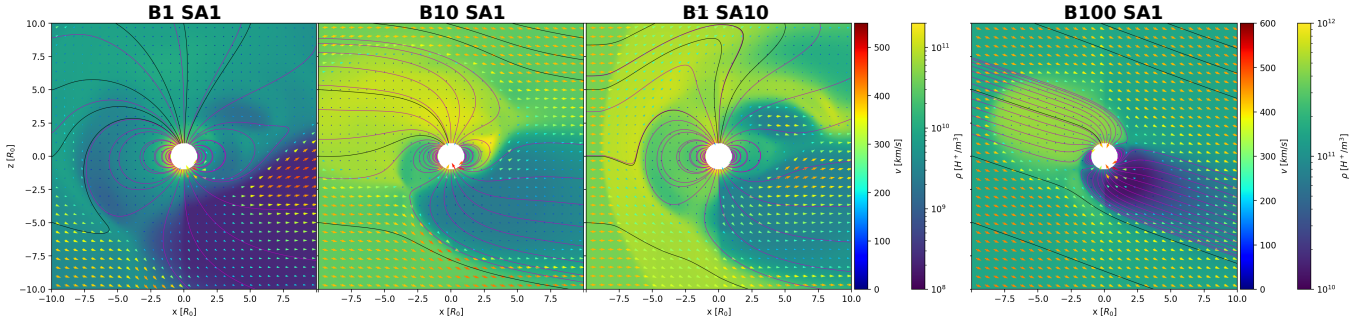


Figure 8. xz -plane cross sections of the magnetosphere of τ Boötis Ab. Velocity vectors and respective magnitudes are indicated by arrows (km/s, left colorbar). Color contours indicate plasma mass density (H^+ /m³, right colorbar). Black and magenta lines depict magnetic field line projections into the xz -plane.

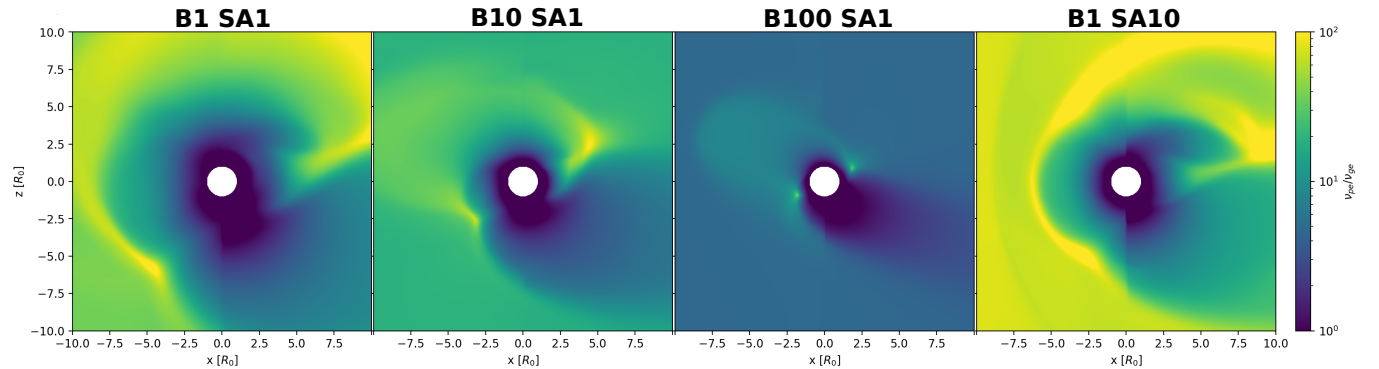


Figure 9. Electron plasma-to-gyro frequency ratio f_p/f_c within the xz -plane parallel to the planetary dipole axis. A value $f_p/f_c > 1$ indicates that emission can escape the respective region.

however, would not shift the expected radio flux into the observed range.

7 CONCLUSIONS

In this work we have presented a three-dimensional magnetohydrodynamical wind model based on spectropolarimetric observations made at the same time as the radio detections in the τ Boötis system.

To account for transient variation in wind power and uncertainty surrounding the absolute magnetic field strength of τ Boötis A, we have created four different stellar wind models. The first three models (B1, B10, and B100) have their magnetic field scaled by a factor of 1, 10, and 100, respectively. An additional model, SA10, where the Alfvén flux-to-field ratio is scaled by a factor of 10, is also presented. The wind models extend from the stellar chromosphere past the orbit of τ Boötis Ab. We find that the planet orbits in the transalfvénic regime in the B1 model, in the super-alfvénic regime for B10 and B100, and in the sub-alfvénic regime for the SA10 model.

For each of our model cases we trace the Alfvén characteristics backward and forwards from the planetary magnetosphere, revealing different energy paths for the flow of Alfvén wave energy in the sub-alfvénic and super-alfvénic regimes.

We have computed the expected radio emissions from the system based on electron cyclotron maser instability (ECMI) emissions as well as the background thermal bremsstrahlung. In our models we find that the emission intensity scales slightly superlinearly with the magnetic field strength, and is not strongly affected by the Poynting

flux-to-field ratio which controls the flux of Alfvén wave energy into the chromosphere. We find that a moderate scaling of the magnetic field by a factor of ~ 10 is required to match the slowly varying signal reported by Turner et al. (2021), and that a scaling of ~ 40 is required to match the mean intensity of the bursty signal. A larger conversion efficiency (η value) and a different beaming factor can, however, bring the required scaling down to ~ 1 (i.e. no scaling) for the slowly varying signal and a factor of ~ 4 for the bursty signal.

Given the suggested 100–1000 times flux variations suggested by Farrell et al. (1999), it may be that both a temporary surge of wind power and favourable viewing geometry is required to attain the flux levels reported by Turner et al. (2021). Since wind variations are difficult to predict, they would add an element of unpredictability to the detection of exoplanetary radio signals, and may be the reason why follow-up observations of τ Boötis Ab have not yielded positive detections.

ACKNOWLEDGEMENTS

This project has received funding from the European Research Council (ERC) under the European Union’s Horizon 2020 research and innovation programme (grant agreement No 817540, ASTROFLOW and No. 884711, Exo-Oceans). This publication is part of the projects OCENW.M.22.215 (under research programme Open Competition Domain Science - M) and VI.C.232.041 (under research programme Talent Programme Vici), which are financed by the Dutch Research Council (NWO). We thank SURF (www.surf.nl) for the support in

using the National Supercomputer Snellius and the **Gauss Centre for Supercomputing e.V.** (www.gauss-centre.eu) for funding this project by providing computing time through the John von Neumann Institute for Computing (NIC) on the GCS Supercomputer JUWELS at Jülich Supercomputing Centre (JSC). This work was carried out using the SWMF and BATS-R-US tools developed at the University of Michigan's **Center for Space Environment Modeling (CSEM)**. The modeling tools are available through the University of Michigan for download under a user license; an open source version is available at <https://github.com/SWMFsoftware>. This research has made use of NASA's **Astrophysics Data System**. This work has made use of the following additional numerical software, statistics software and visualisation software: NumPy ([van der Walt et al. 2011](#)), SciPy ([Virtanen et al. 2020](#)), Matplotlib ([Hunter 2007](#)), Tecplot, and PyTecplot.

DATA AVAILABILITY

The data underlying this article will be shared on reasonable request to the corresponding author.

REFERENCES

- Acuna M. H., Ness N. F., 1976, *J. Geophys. Res.*, **81**, 2917
- Alvarado-Gómez J. D., Hussain G. A. J., Cohen O., Drake J. J., Garraffo C., Grunhut J., Gombosi T. I., 2016a, *A&A*, **588**, A28
- Alvarado-Gómez J. D., Hussain G. A. J., Cohen O., Drake J. J., Garraffo C., Grunhut J., Gombosi T. I., 2016b, *A&A*, **594**, A95
- Alvarado-Gómez J. D., et al., 2020, *ApJ*, **895**, 47
- Aurière M., 2003, in Arnaud J., Meunier N., eds, EAS Publications Series Vol. 9, EAS Publications Series, p. 105
- Bastian T. S., Dulk G. A., Leblanc Y., 2000, *ApJ*, **545**, 1058
- Baumjohann W., Treumann R. A., 2012, Basic Space Plasma Physics (Revised Edition), doi:10.1142/p850.
- Bode J. E., 1768, Anleitung zur Kenntniss des gestirnten Himmels, doi:10.3931/e-rara-1429.
- Borsa F., et al., 2015, *A&A*, **578**, A64
- Brogi M., Snellen I. A. G., de Kok R. J., Albrecht S., Birkby J., de Mooij E. J. W., 2012, *Nature*, **486**, 502
- Butler R. P., Marcy G. W., Williams E., Hauser H., Shirts P., 1997, *ApJ*, **474**, L115
- Butler R. P., et al., 2006, *ApJ*, **646**, 505
- Callingham J. R., et al., 2024, arXiv e-prints, p. arXiv:2409.15507
- Catala C., Donati J.-F., Shkolnik E., Bohlender D., Alecian E., 2007, *MNRAS*, **374**, L42
- Chapman S., Ferraro V. C. A., 1930, *Nature*, **126**, 129
- Chapman S., Ferraro V. C. A., 1931, *Terrrestrial Magnetism and Atmospheric Electricity (Journal of Geophysical Research)*, **36**, 77
- Christensen U. R., Holzwarth V., Reiners A., 2009, *Nature*, **457**, 167
- Cohen O., 2017, *ApJ*, **835**, 220
- Cohen O., Moschou S.-P., Glocer A., Sokolov I. V., Mazeh T., Drake J. J., Garraffo C., Alvarado-Gómez J. D., 2018, *AJ*, **156**, 202
- Connerney J. E. P., 1993, *J. Geophys. Res.*, **98**, 18659
- Cordin C. M., Vedantham H. K., Brentjens M. A., van der Tak F. F. S., 2025, arXiv e-prints, p. arXiv:2501.06301
- Cravens T. E., 2004, Physics of Solar System Plasmas
- Desch M. D., Kaiser M. L., 1984, *Nature*, **310**, 755
- Donati J. F., Landstreet J. D., 2009, *ARA&A*, **47**, 333
- Donati J.-F., Semel M., Carter B. D., Rees D. E., Collier Cameron A., 1997, *MNRAS*, **291**, 658
- Donati J.-F., et al., 2006, *MNRAS*, **370**, 629
- Donati J.-F., et al., 2008, *MNRAS*, **385**, 1179
- Drell S. D., Foley H. M., Ruderman M. A., 1965, *J. Geophys. Res.*, **70**, 3131
- Elekes F., Saur J., 2023, *A&A*, **671**, A133
- Elsasser W. M., 1950, *Physical Review*, **79**, 183
- Evensberget D., Vidotto A. A., 2024, *MNRAS*, **529**, L140
- Evensberget D., Carter B. D., Marsden S. C., Brookshaw L., Folsom C. P., 2021, *MNRAS*, **506**, 2309
- Evensberget D., Carter B. D., Marsden S. C., Brookshaw L., Folsom C. P., Salmeron R., 2022, *MNRAS*, **510**, 5226
- Evensberget D., et al., 2023, *MNRAS*, **524**, 2042
- Fares R., et al., 2009, *MNRAS*, **398**, 1383
- Fares R., Moutou C., Donati J. F., Catala C., Shkolnik E. L., Jardine M. M., Cameron A. C., Deleuil M., 2013, *MNRAS*, **435**, 1451
- Farrell W. M., Desch M. D., Zarka P., 1999, *J. Geophys. Res.*, **104**, 14025
- Fleishman G. D., Kuznetsov A. A., Landi E., 2021, *ApJ*, **914**, 52
- Franklin K. L., Burke B. F., 1958, *J. Geophys. Res.*, **63**, 807
- Gaia Collaboration et al., 2023, *A&A*, **674**, A1
- Garraffo C., Drake J. J., Cohen O., Alvarado-Gómez J. D., Moschou S. P., 2017, *ApJ*, **843**, L33
- Gombosi T. I., van der Holst B., Manchester W. B., Sokolov I. V., 2018, *Living Reviews in Solar Physics*, **15**, 4
- Gombosi T. I., et al., 2021, *Journal of Space Weather and Space Climate*, **11**, 42
- Grießmeier J. M., Motschmann U., Mann G., Rucker H. O., 2005, *A&A*, **437**, 717
- Grießmeier J. M., Zarka P., Spreeuw H., 2007, *A&A*, **475**, 359
- Hallinan G., et al., 2015, *Nature*, **523**, 568
- Hess S., Cecconi B., Zarka P., 2008, *Geophys. Res. Lett.*, **35**, L13107
- Hess S. L. G., Pétin A., Zarka P., Bonfond B., Cecconi B., 2010, *Planet. Space Sci.*, **58**, 1188
- Hill T. W., 2001, *J. Geophys. Res.*, **106**, 8101
- Hunter J. D., 2007, *Computing in Science and Engineering*, **9**, 90
- Jardine M., Barnes J. R., Donati J.-F., Collier Cameron A., 1999, *MNRAS*, **305**, L35
- Johnstone C. P., Güdel M., 2015, *A&A*, **578**, A129
- Justesen A. B., Albrecht S., 2019, *A&A*, **625**, A59
- Kavanagh R. D., Vedantham H. K., 2023, *MNRAS*, **524**, 6267
- Kavanagh R. D., et al., 2019, *MNRAS*, **485**, 4529
- Kavanagh R. D., Vidotto A. A., Klein B., Jardine M. M., Donati J.-F., Ó Fionnagáin D., 2021, *MNRAS*, **504**, 1511
- Kilmetis K., Vidotto A. A., Allan A., Kubyshkina D., 2024, *MNRAS*, **535**, 3646
- Kivelson M. G., Russell C. T., 1995, Introduction to Space Physics. Cambridge University Press
- Kochukhov O., Makaganiuk V., Piskunov N., 2010, *A&A*, **524**, A5
- Lammer H., et al., 2007, *Astrobiology*, **7**, 185
- Lazio T. J. W., Farrell W. M., 2007, *ApJ*, **668**, 1182
- Lazio T. Joseph W., Farrell W. M., Dietrick J., Greenlees E., Hogan E., Jones C., Hennig L. A., 2004, *ApJ*, **612**, 511
- Lee J., 2007, *Space Sci. Rev.*, **133**, 73
- Lockwood A. C., Johnson J. A., Bender C. F., Carr J. S., Barman T., Richert A. J. W., Blake G. A., 2014, *ApJ*, **783**, L29
- Marsden S. C., et al., 2023, *MNRAS*, **522**, 792
- McIntyre S. R. N., Lineweaver C. H., Ireland M. J., 2019, *MNRAS*, **485**, 3999
- Melrose D. B., 1989, Instabilities in Space and Laboratory Plasmas
- Meng X., van der Holst B., Tóth G., Gombosi T. I., 2015, *MNRAS*, **454**, 3697
- Mengel M. W., et al., 2016, *MNRAS*, **459**, 4325
- Moschou S.-P., Sokolov I., Cohen O., Drake J. J., Borovikov D., Kasper J. C., Alvarado-Gómez J. D., Garraffo C., 2018, *ApJ*, **867**, 51
- Neubauer F. M., 1998, *J. Geophys. Res.*, **103**, 19843
- Nicholson B. A., et al., 2016, *MNRAS*, **459**, 1907
- Nindos A., Aurass H., Klein K. L., Trottet G., 2008, *Sol. Phys.*, **253**, 3
- Nindos A., Kontar E. P., Oberoi D., 2019, *Advances in Space Research*, **63**, 1404
- O'Fionnagáin D., 2021, radiowinds: Radio emission from stellar winds, Astrophysics Source Code Library, record ascl:2101.004
- Ó Fionnagáin D., et al., 2019, *MNRAS*, **483**, 873
- Ó Fionnagáin D., Kavanagh R. D., Vidotto A. A., Jeffers S. V., Petit P., Marsden S., Morin J., Golden A., 2022, *ApJ*, **924**, 115
- Pope B. J. S., Withers P., Callingham J. R., Vogt M. F., 2019, *MNRAS*, **484**, 648
- Poppenhaeger K., Robrade J., Schmitt J. H. M. M., 2010, *A&A*, **515**, A98

- Powell K. G., Roe P. L., Linde T. J., Gombosi T. I., De Zeeuw D. L., 1999, *Journal of Computational Physics*, **154**, 284
- Presa A., Driessen F. A., Vidotto A. A., 2024, *MNRAS*,
- Reiners A., Schüssler M., Passegger V. M., 2014, *ApJ*, **794**, 144
- Renard S., Absil O., Berger J. P., Bonfils X., Forveille T., Malbet F., 2008, in Schöller M., Danchi W. C., Delplancke F., eds, Society of Photo-Optical Instrumentation Engineers (SPIE) Conference Series Vol. 7013, Optical and Infrared Interferometry. p. 70132Z ([arXiv:0807.3014](#)), doi:[10.1117/12.790494](#)
- Rodler F., Lopez-Morales M., Ribas I., 2012, *ApJ*, **753**, L25
- Rosenthal L. J., et al., 2021, *ApJS*, **255**, 8
- Russell C. T., 1978, *Nature*, **272**, 147
- Russell C. T., Luhmann J. G., Strangeway R. J., 2016, Space Physics: An Introduction
- Rybicki G. B., Lightman A. P., 1986, Radiative Processes in Astrophysics
- Sachdeva N., et al., 2019, *ApJ*, **887**, 83
- Saur J., 2018, in Deeg H. J., Belmonte J. A., eds, , Handbook of Exoplanets. p. 27, doi:[10.1007/978-3-319-55333-7_27](#)
- Saur J., Grambusch T., Duling S., Neubauer F. M., Simon S., 2013, *A&A*, **552**, A119
- Saur J., Willmes C., Fischer C., Wenmacher A., Roth L., Youngblood A., Strobel D. F., Reiners A., 2021, *A&A*, **655**, A75
- Seach J. M., Marsden S. C., Carter B. D., Evensberget D., Folsom C. P., Neiner C., Mengel M. W., 2022, *MNRAS*, **509**, 5117
- Semel M., 1989, *A&A*, **225**, 456
- Shkolnik E., Walker G. A. H., Bohlender D. A., Gu P. G., Kürster M., 2005, *ApJ*, **622**, 1075
- Shkolnik E., Bohlender D. A., Walker G. A. H., Collier Cameron A., 2008, *ApJ*, **676**, 628
- Siscoe G. L., Chen C. K., 1975, *J. Geophys. Res.*, **80**, 4675
- Skilling J., Bryan R. K., 1984, *MNRAS*, **211**, 111
- Sokolov I. V., et al., 2013, *ApJ*, **764**, 23
- Strickert K. M., Evensberget D., Vidotto A. A., 2024, *MNRAS*, **533**, 1156
- Strugarek A., Brun A. S., Matt S. P., Réville V., 2015, *ApJ*, **815**, 111
- Tarduno J. A., et al., 2010, *Science*, **327**, 1238
- Tóth G., et al., 2005, *Journal of Geophysical Research (Space Physics)*, **110**, A12226
- Tóth G., et al., 2012, *Journal of Computational Physics*, **231**, 870
- Treumann R. A., 2006, *A&ARv*, **13**, 229
- Turner J. D., et al., 2021, *A&A*, **645**, A59
- Turner J. D., et al., 2023, *arXiv e-prints*, p. [arXiv:2310.05363](#)
- Turner J. D., Grießmeier J.-M., Zarka P., Zhang X., Mauduit E., 2024, *A&A*, **688**, A66
- Turnpenney S., Nichols J. D., Wynn G. A., Burleigh M. R., 2018, *ApJ*, **854**, 72
- Twiss R. Q., 1958, *Australian Journal of Physics*, **11**, 564
- Vidotto A. A., Donati J. F., 2017, *A&A*, **602**, A39
- Vidotto A. A., Opher M., Jatenco-Pereira V., Gombosi T. I., 2009, *ApJ*, **703**, 1734
- Vidotto A. A., Opher M., Jatenco-Pereira V., Gombosi T. I., 2010, *ApJ*, **720**, 1262
- Vidotto A. A., Llama J., Jardine M., Helling C., Wood K., 2011, *Astronomische Nachrichten*, **332**, 1055
- Vidotto A. A., Fares R., Jardine M., Donati J.-F., Opher M., Moutou C., Catala C., Gombosi T. I., 2012, *MNRAS*, **423**, 3285
- Vidotto A. A., Jardine M., Morin J., Donati J. F., Lang P., Russell A. J. B., 2013, *A&A*, **557**, A67
- Virtanen P., et al., 2020, *Nature Methods*, **17**, 261
- Wang J., Ford E. B., 2011, *MNRAS*, **418**, 1822
- Weber C., et al., 2017, *MNRAS*, **469**, 3505
- Weber C., Erkaev N. V., Ivanov V. A., Odert P., Grießmeier J. M., Fossati L., Lammer H., Rucker H. O., 2018, *MNRAS*, **480**, 3680
- White S. M., Kundu M. R., 1997, *Sol. Phys.*, **174**, 31
- Wood B. E., et al., 2021, *ApJ*, **915**, 37
- Wu C. S., Lee L. C., 1979, *ApJ*, **230**, 621
- Zarka P., 1998, *J. Geophys. Res.*, **103**, 20159
- Zarka P., 2007, *Planet. Space Sci.*, **55**, 598

Table A1. Time and phase for the spectropolarimetric observations used to construct the stellar magnetic map. The times of the observations are given in coordinated universal time (UTC) and Julian date (JD). The cycle phase and stellar longitude of each observations is computed using the reference Julian date 2 453 450.984.

UTC	Julian date	Cycle Phase	Longitude
2017-02-15 05:06	2 457 799.713 00	0.8154	66.5
2017-02-16 05:05	2 457 800.712 17	0.1173	317.8
2017-02-17 03:30	2 457 801.645 94	0.3994	216.2
2017-02-18 03:22	2 457 802.640 60	0.6999	108.0
2017-02-19 03:19	2 457 803.638 36	0.0013	359.5
2017-02-20 03:53	2 457 804.661 88	0.3105	248.2
2017-02-22 03:49	2 457 806.659 54	0.9141	30.9

- Zarka P., 2010, in Coudé du Foresto V., Gelino D. M., Ribas I., eds, Astronomical Society of the Pacific Conference Series Vol. 430, Pathways Towards Habitable Planets. p. 175
- Zarka P., Treumann R. A., Ryabov B. P., Ryabov V. B., 2001, *Ap&SS*, **277**, 293
- Zarka P., Cecconi B., Kurth W. S., 2004, *Journal of Geophysical Research (Space Physics)*, **109**, A09S15
- Zarka P., Marques M. S., Louis C., Ryabov V. B., Lamy L., Echer E., Cecconi B., 2018, *A&A*, **618**, A84
- Zarka P., Louis C. K., Zhang J., Tian H., Morin J., Gao Y., 2025, *arXiv e-prints*, p. [arXiv:2501.16180](#)
- van Haarlem M. P., et al., 2013, *A&A*, **556**, A2
- van der Holst B., Sokolov I. V., Meng X., Jin M., Manchester W. B. I., Tóth G., Gombosi T. I., 2014, *The Astrophysical Journal*, **782**, 81
- van der Holst B., Manchester W. B. I., Klein K. G., Kasper J. C., 2019, *ApJ*, **872**, L18
- van der Walt S., Colbert S. C., Varoquaux G., 2011, *Computing in Science and Engineering*, **13**, 22

APPENDIX A: SPECTROPOLARIMETRIC OBSERVATIONS

Table A1 lists the spectropolarimetric observations used to construct the stellar magnetic map. The times of the observations are given in coordinated universal time (UTC) and Julian date (JD). The cycle phase and stellar longitude of each observations is computed using the reference Julian date 2 453 450.984 and the stellar rotation period 3.31.

APPENDIX B: ALFVEN SURFACE PLOT

Fig. B1 shows the wind radial velocity, Alfvén surface, and magnetic current sheet for the four model cases of Table 2. The planetary orbit is indicated as a white circle. The Alfvén surface can be seen to increase with the magnetic field strength, and shrink with increased Poynting flux.

APPENDIX C: THERMAL BREMSSTRAHLUNG AT 30 MHz

Fig. C1 shows the thermal bremsstrahlung at 30 MHz. The figure is similar to Fig. 5, but the thermal bremsstrahlung is computed for a frequency of 30 MHz instead of for 10 MHz. Notably the optically thick region is smaller than at 10 MHz, while the emission strength is greater (viz. Fig. 5).

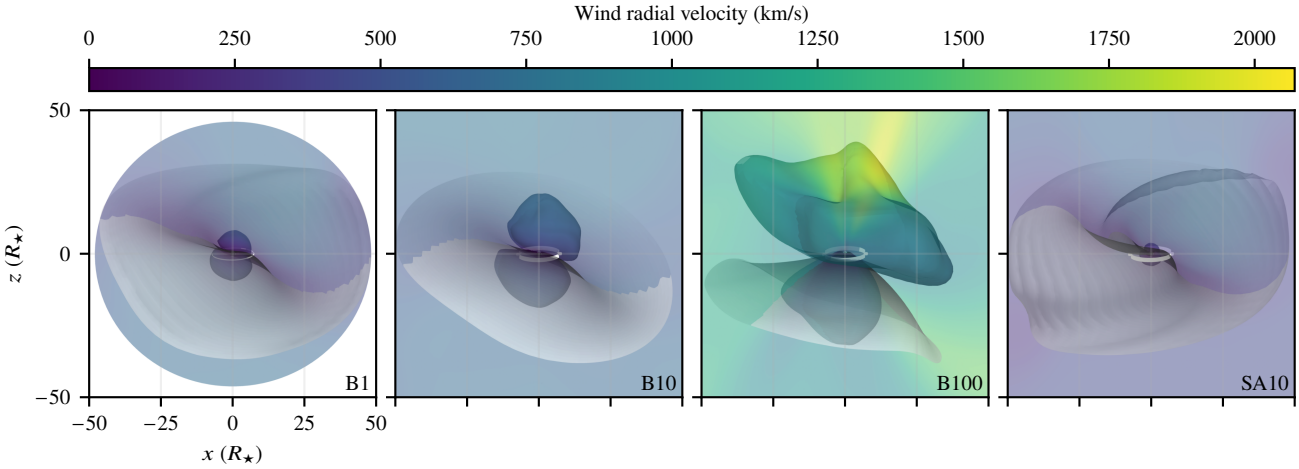


Figure B1. Wind radial velocity, Alfvén surface, and magnetic current sheet for the four model cases of Table 2. The planetary orbit is indicated as a white circle. The Alfvén surface can be seen to increase with the magnetic field strength, and shrink with increased Poynting flux.

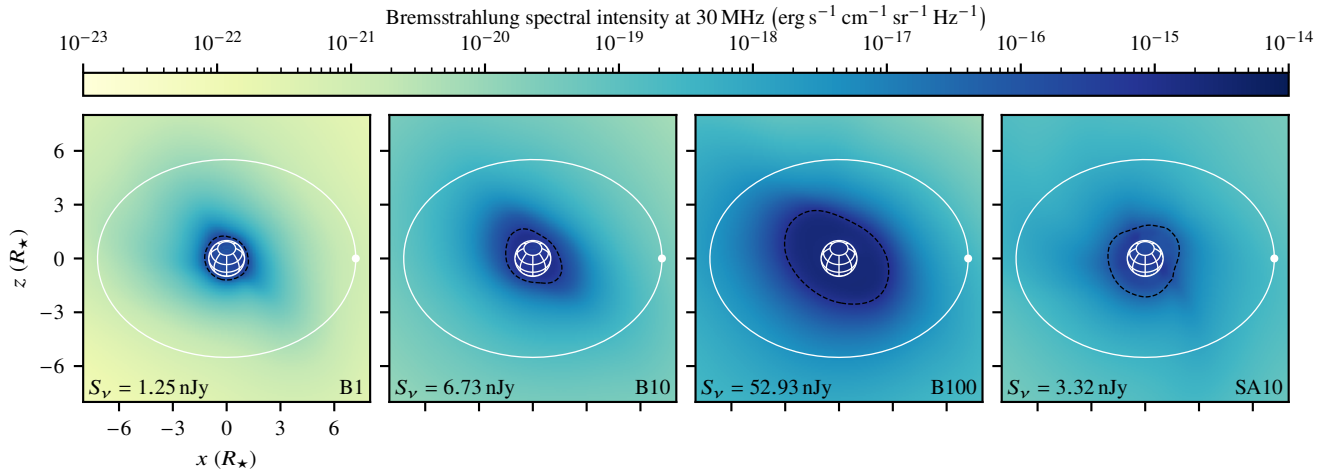


Figure C1. Thermal bremsstrahlung at 30 MHz. This figure is similar to Fig. 5, but the thermal bremsstrahlung is computed for a frequency of 30 MHz. Notably the optically thick region is smaller than at 10 MHz, and the emission strength is greater than at 30 MHz (viz. Fig. 5).

APPENDIX D: DIPOLAR PLANETARY MAGNETIC FIELD

Assuming that the planet's magnetic field is dipolar, the planetary magnetic field is given by

$$\mathbf{B}(\mathbf{r}) = \frac{\mu_0}{4\pi} \left(\frac{3\mathbf{r}(\mathbf{m} \cdot \mathbf{r})}{r^5} - \frac{\mathbf{m}}{r^3} \right) \quad (\text{D1})$$

where \mathbf{m} is the dipole magnetic moment of the planet. By defining α as the angle between \mathbf{m} and \mathbf{r} , $m v \cos \alpha = \mathbf{m} \cdot \mathbf{v}$, and taking the magnitude of equation (D1) we find that the the planetary magnetic field strength is

$$B(r, \alpha) = \frac{\mu_0 m}{4\pi r^3} \sqrt{1 + 3 \cos^2 \alpha},$$

We can relate m to the surface magnetic field strength at the planet's surface. At the planet's magnetic pole ($R_p, 0^\circ$) we define $B_p = B(R_p, 0^\circ)$. This sets the magnetic moment m as

$$m = (2\pi/\mu_0) B_p R_p^3,$$

where R_p is the planet's radius and r is the distance from the planet's centre. With the magnetic moment m thus expressed, we can express

the magnetic field strength at any point (r, α) as a function of B_p :

$$B(r, \alpha) = \frac{B_p}{2} \left(\frac{R_p^3}{r} \right) \sqrt{1 + 3 \cos^2 \alpha}. \quad (\text{D2})$$

We see from the square root term that $B(r, \alpha)$ varies by a factor of 2 between the magnetic pole, where $\alpha = 0^\circ$ and the magnetic equator, where $\alpha = 90^\circ$ for all distances r .

D1 Magnetospheric size

The planet-produced pressure is calculated analytically based on a number of simplifying assumptions. We assume that the planet-produced pressure is dominated by the magnetic pressure. From eq. (D2) we see that the magnetic field over the surface scales as $B(r, \alpha) = (R_p/r)^3 B(R_p, \alpha)$. The planet-produced pressure is then given by

$$p_p(r, \alpha) = \frac{1}{2\mu_0} B(r, \alpha)^2 = \frac{1}{2\mu_0} \frac{B_p^2}{4} \left(\frac{R_p}{r} \right)^6 \left(1 + 3 \cos^2 \alpha \right).$$

Equating the wind pressure p_w to the planet-produced pressure p_p and solving for r gives an indication of the size of the planetary magnetosphere R_{mag} ,

$$\frac{R_{\text{mag}}}{R_p} = \left(\frac{1}{2\mu_0} \frac{B_p^2}{p_w} \right)^{1/6} \left(\frac{1 + 3 \cos^2 \alpha}{4} \right)^{1/6} \simeq \left(\frac{1}{2\mu_0} \frac{B_p^2}{p_w} \right)^{1/6}.$$

The geometric term containing α varies from 0.79 to 0.89. We note that for superalfvénic flow a term ξ is often included to account for the effects of electrical currents in the magnetopause (Cravens 2004). The term $\xi = 2^{1/3}$ is used in Vidotto et al. (2011).

D2 The size of the polar cap/auroral region

The auroral region is a ring-shaped region around the magnetic poles of the planet. The outer boundary of the auroral ring is thought to be the boundary between open and closed planetary magnetic field lines, i.e. magnetic field lines with one (open) or both (closed) ends connected to the planet (Hill 2001). This region is also referred to as the polar cap (Tarduno et al. 2010; Vidotto et al. 2013).

Since the dipolar magnetic field of the planet is disturbed by the stellar wind beyond the magnetopause distance R_{mag} we can trace the dipolar planetary magnetic field lines to see whether they extend past R_{mag} , in which case they may connect with the magnetic field embedded in the stellar wind. Given that the distance to the magnetopause is R_{mag} , the polar cap is the region where the magnetic field lines extend past R_{mag} .

We consider the dipolar magnetic field of eq. (D1). Using coordinates where $\mathbf{m} \parallel \hat{\mathbf{z}}$ we have

$$B_x = \frac{\mu_0}{4\pi} (3mxz)/r^5 \quad \text{and} \quad B_z = \frac{\mu_0}{4\pi} (2mz^2 - x^2)/r^5.$$

The magnetic field lines in the xz plane are described by

$$\frac{dz}{dx} = \frac{B_z}{B_x} = \frac{2z^2 - x^2}{3xz},$$

which is a Bernoulli differential equation with a family of solutions parametrised by r_0 :

$$z = \pm \sqrt{r_0^{2/3} x^{4/3} - x^2},$$

with each value of r_0 giving rise to a different field line. Along each field line in the xz plane $r^2 = x^2 + z^2 = r_0^{2/3} x^{4/3}$, and thus

$$r = r_0 \sin^2 \alpha \tag{D3}$$

by cylindrical symmetry, where we used $x = r \sin \alpha$ with α being the colatitude or polar angle. We see that r_0 is the maximum distance reached by the fieldline, reached when $\alpha = 90^\circ$, i.e. in the magnetic equatorial plane.

To find the colatitude of the polar cap α_{cap} we find the α value at $r = R_p$ for the field line that reaches $r_0 = R_{\text{mag}}$, i.e. where $R_p = R_{\text{mag}} \sin^2 \alpha_{\text{cap}}$ by eq. (D3). This gives

$$\alpha_{\text{cap}} = \arcsin \sqrt{R_p/R_{\text{mag}}} \tag{D4}$$

as given in e.g. Vidotto et al. (2011).

APPENDIX E: BEAMED EMISSION

Independent on the mechanism powering ECMI, the power is emitted locally in a thin, hollow cone. To find the solid angle spanned by this shape C we consider the difference between two cones C_1 and C_2

with half-opening angles α_1 and α_2 , respectively, and $\alpha_1 > \alpha_2$. The solid angle spanned by C_i is that of a spherical cap (see also Vidotto & Donati 2017)

$$\Omega_{C_i} = 2\pi(1 - \cos \alpha_i), \tag{E1}$$

and the solid angle spanned by $C = C_1 - C_2$ is thus

$$\Omega_C = \Omega_{C_1} - \Omega_{C_2} = 2\pi(\cos \alpha_2 - \cos \alpha_1).$$

By furthermore writing $\alpha = (\alpha_1 + \alpha_2)/2$ and $\Delta\alpha = \alpha_1 - \alpha_2$, we can write

$$\Omega_C = 4\pi \sin(\alpha) \sin(\Delta\alpha/2).$$

where we have used the angle addition formula $\cos(a \pm b) = \cos a \cos b \mp \sin a \sin b$.

E1 Unresolved double cone

Since the power is emitted in both the northern and southern hemisphere, the final solid angle is

$$\Omega_{\text{radio}} = 2\Omega_C = 8\pi \sin(\alpha) \sin(\Delta\alpha/2).$$

Where α is the hollow cone's half-opening angle and $\Delta\alpha$ is its thickness. This is used in equation (10) of the main paper.

This paper has been typeset from a $\text{\TeX}/\text{\LaTeX}$ file prepared by the author.